https://doi.org/10.5194/egusphere-2025-4277
Preprint. Discussion started: 21 October 2025

Improving Thermodynamic Nudging in the E3SM Atmosphere Model Version 2 (EAMv2): Strategy and Hindcast Skills on Weather Systems

Shixuan Zhang[1], L. Ruby Leung[1], Bryce E. Harrop[1], Aniruddha Bora[2], George Karniadakis[2], Khemraj Shukla[2], and Kai Zhang[1]

[1]Atmospheric, Climate, and Earth Sciences Division, Pacific Northwest National Laboratory, Richland, WA 99354, USA
[2]Division of Applied Mathematics, Brown University, Providence, RI 02912, USA

Correspondence: Shixuan Zhang (shixuan.zhang@pnnl.gov) and L. Ruby Leung (ruby.leung@pnnl.gov)

Abstract. Nudging techniques are commonly employed to constrain atmospheric simulations toward observed states, facilitating model evaluation and sensitivity studies. However, if applied improperly—particularly to thermodynamic variables such as temperature and humidity—nudging can distort physical processes and introduce spurious biases, undermining the credibility of the simulations. This study presents an improved nudging implementation that applies vertically modulated tendencies to reduce adverse impacts on model physics. The framework is tested in version 2 of the Energy Exascale Earth System Model (EAMv2) using a suite of hindcast simulations nudged toward ERA5 reanalysis. We systematically evaluate the individual and combined effects of nudging wind, temperature, and humidity fields on the model's ability to represent large-scale atmospheric states and high-impact weather systems. Results show that the revised strategy—particularly when nudging temperature and humidity at selected levels—enhances hindcast skill by improving agreement with ERA5 without degrading the hydrological cycle or precipitation processes. Additional improvements in surface temperature, outgoing longwave radiation, and precipitation biases are achieved through targeted nudging of land surface variables. The proposed approach strengthens the representation of large-scale conditions relevant to tropical cyclones, atmospheric rivers, and extratropical cyclones in the low-resolution EAMv2. These findings demonstrate that carefully designed thermodynamic nudging, especially of temperature and humidity, improves the realism of constrained simulations and broadens the utility of nudged EAMv2 for atmospheric modeling, machine learning, and high-impact weather research.

1 Introduction

Nudging is a data assimilation method widely used to adjust dynamical variables of general circulation models (GCMs) toward meteorological reanalysis data, producing realistic representations of weather systems in long-term simulations. Such approaches enable the evaluation of model biases by allowing direct comparison between simulations and observations (e.g., Jeuken et al., 1996; Separovic et al., 2012; Lohmann and Hoose, 2009; Ma et al., 2015; Lin et al., 2016). They also enhance the signal-to-noise ratio in sensitivity experiments, allowing estimation of model responses to external forcing without requiring long integrations or large ensembles (e.g., Zhang et al., 2012; Kooperman et al., 2012; Zhang et al., 2022a). Despite

https://doi.org/10.5194/egusphere-2025-4277
Preprint. Discussion started: 21 October 2025

these advantages, the success of nudged atmospheric hindcasts depends critically on the design of nudging strategies tailored to the model and research objectives. In terms of the constrained quantities, which include large-scale dynamical (zonal and meridional winds) and thermodynamical (temperature and humidity) fields, many studies have shown that directly nudging temperature and humidity can distort the simulated atmospheric state and fluxes. This reduces the usefulness of bias evaluation and the estimation of model responses to external forcing (Jeuken et al., 1996; Zhang et al., 2014; Ma et al., 2015; Sun et al., 2019; Zhang et al., 2022b). As a result, wind-only nudging is often recommended for constrained hindcast experiments (e.g., Sun et al., 2019; Zhang et al., 2022b).

However, there are cases where temperature and humidity nudging is advantageous or even necessary for model evaluation and applications. For example, Watt-Meyer et al. (2021) and Bretherton et al. (2021) used nudging to generate numerical training datasets for developing machine learning bias correction models. In this context, all state variables, including wind, temperature, and humidity, must be constrained toward the real atmosphere to enable realistic estimation of model biases across seasons and the diurnal cycle, which is essential for successful training. Similarly, Wehrli et al. (2018, 2019, 2022) designed experiments with atmospheric nudging to investigate the relative roles of thermodynamic and dynamic processes in biased simulations of extreme atmospheric events. In studies of this kind, dynamic and thermodynamic contributions to model biases are separated by nudging subsets of large-scale wind (dynamics), temperature, and humidity (thermodynamics) fields toward observed atmospheric profiles. Such experimental approaches, however, may become less reliable if nudging of temperature and humidity introduces spurious biases or unrealistic fields, as reported in previous studies (Jeuken et al., 1996; Zhang et al., 2014; Sun et al., 2019; Zhang et al., 2022b).

Motivated by the emerging need for temperature and humidity nudging in model analysis and evaluation, this study extends the work of Sun et al. (2019) and Zhang et al. (2022b) on atmospheric nudging within the Energy Exascale Earth System Model atmosphere component (EAM; Rasch et al., 2019; Xie et al., 2018; Leung et al., 2020; Golaz et al., 2019, 2022). We focus on developing strategies that incorporate temperature and humidity, in addition to large-scale wind fields, to improve the realism of atmospheric simulations nudged toward reanalysis products while avoiding significant drifts in other fields important for evaluation, such as precipitation and radiative fluxes. Our goal is to demonstrate that this enhanced nudging approach enables more reliable, constrained hindcast simulations that are especially valuable for high-impact weather analysis and for machine learning applications using low-resolution models such as EAM. These aspects of nudging strategy and application remain underexplored in previous EAM-based studies (e.g., Sun et al., 2019; Zhang et al., 2022b).

The remainder of this manuscript is organized as follows. Section 2 describes the implementation of a modified nudging tendency scheme in version 2 of the EAM (EAMv2). Section 3 examines the limitations of the default temperature and humidity nudging strategy in EAMv2 and introduces the revised formulation proposed in this study, highlighting its improvements through direct comparison with the original approach. Section 4 evaluates the hindcast performance of EAMv2 simulations with different sets of constrained variables, with particular emphasis on the benefits of the revised temperature and humidity nudging strategy for improving the simulation of long-term precipitation evolution and land–atmosphere interactions. Section 5 presents further analysis of the role of humidity nudging in simulating high-impact weather events using the low-resolution EAM. Finally, Section 6 summarizes the key findings and offers recommendations.

https://doi.org/10.5194/egusphere-2025-4277
Preprint. Discussion started: 21 October 2025

2 Model and Nudging Methodology

2.1 A brief overview of E3SM Atmosphere Model (EAM)

E3SM is a global Earth system model developed by the U.S. Department of Energy (Golaz et al., 2019, 2022). This study uses the E3SM Atmosphere Model version 2 (EAMv2; Golaz et al., 2022) with standard resolution (also referred to as the "low-resolution" configuration). In brief, EAMv2 uses separate grids for dynamics and column physics parameterizations. The dynamical core is configured to run on a cubed-sphere mesh with a quasi-uniform horizontal resolution of 110 km to solve the dynamics and tracer transport (Dennis et al., 2012; Taylor and Fournier, 2010). While the dynamics is solved on the Gauss-Lobato-Legendre quadrature points within each element of the grid, the column physics parameterizations are solved on a simple 2x2 subgrid of quadrilaterals within each element (Lauritzen et al., 2018; Herrington et al., 2019; Hannah et al., 2021). The key subgrid-scale physical parameterizations considered in EAMv2 include deep convection (Zhang and McFarlane, 1995), turbulence and shallow convection (Golaz et al., 2002; Larson et al., 2002), cloud microphysics (Morrison and Gettelman, 2008; Gettelman and Morrison, 2015; Wang et al., 2014), aerosol life cycle (Liu et al., 2016; Wang et al., 2020), and radiation (Iacono et al., 2008; Mlawer et al., 1997). In addition, EAMv2 is interactively coupled with a land model (Oleson et al., 2013) that uses the same "pg2" grid for column parameterizations. All model components in E3SMv2 are configured with 72 layers in the vertical, extending from the Earth's surface to ∼0.02 hPa (∼64 km). The vertical grid spacing is uneven, with the layer thickness typically ranging from 20 m to 100 m near the surface and up to 600 m near the model top.

2.2 Nudging and Modifications in EAMv2

The nudging implementation in EAMv2 builds upon the earlier version described by Sun et al. (2019). In the configuration used for this study, the nudging workflow follows the revised formulation illustrated in Fig. 1a of Zhang et al. (2022a). Specifically, model state variables—such as horizontal winds (U, V), temperature (T), and specific humidity (Q)—are compared to corresponding reference values before the radiation parameterization is called. A relaxation term, derived from this comparison, is introduced into the time integration loop to constrain the model toward the prescribed atmospheric conditions. The prognostic equation incorporating nudging in EAMv2 can be expressed as:

$$\frac{\partial \boldsymbol{X_m}}{\partial t} = \underbrace{\boldsymbol{D}(\boldsymbol{X_m})}_{dyncmis} + \underbrace{\boldsymbol{P}(\boldsymbol{X_m})}_{physics} - \underbrace{\dot{\boldsymbol{R}}}_{nudging} \tag{1}$$

Here, $\boldsymbol{X_m}$ denotes the model state variable within EAMv2. The terms on the right-hand side represent contributions from large-scale dynamics, physical parameterizations, and the nudging-induced correction term $\dot{\boldsymbol{R}}$, respectively. The nudging tendency term in Sun et al. (2019) and Zhang et al. (2022a) is formulated as follows:

$$\dot{\boldsymbol{R}} = -\frac{\boldsymbol{X_m} - \boldsymbol{X_r}}{\tau} \tag{2}$$

where $\boldsymbol{X_m}$ is referred to as a model state variable (i.e., U, V, T, Q) for EAMv2, while $\boldsymbol{X_r}$ denotes the state in the corresponding reference dataset, often provided by weather analysis products such as ERA5 from the European Centre for Medium-Range

https://doi.org/10.5194/egusphere-2025-4277
Preprint. Discussion started: 21 October 2025

Weather Forecasts (ECMWF). In this study, we proposed to reformulate Eq. (2) as

$$\dot{\boldsymbol{R}} = \begin{cases} 0, & \text{if } P_m \leq 1 \text{ Pa} \\ -\dfrac{\boldsymbol{X_m} - \boldsymbol{X_r}}{\tau} \times \dfrac{P_m}{P_0}, & \text{if } 1 \text{ Pa} < P_m \leq P_0 \\ -\dfrac{\boldsymbol{X_m} - \boldsymbol{X_r}}{\tau} \times \dfrac{1}{2}\left[1 + \tanh\left(\dfrac{Z_m - Z_b}{0.1 * Z_b}\right)\right], & \text{if } Z_m \leq Z_b \\ -\dfrac{\boldsymbol{X_m} - \boldsymbol{X_r}}{\tau}, & \text{otherwise} \end{cases} \tag{3}$$

where P_m and Z_m denote the pressure and geopotential height at the midpoints of the model layers, respectively. Z_b represents the planetary boundary layer (PBL) height, and P_0 is a user-defined threshold parameter for pressure, as described in Table 2. Distinct from the conventional formulation given in Eq.(2), Eq.(3) introduces three additional terms to enable a more nuanced treatment of nudging tendencies across vertical model levels. These modifications are motivated by two key considerations.

First, the vertical extent of EAMv2 reaches up to approximately 0.02 hPa, whereas most widely used reanalysis datasets (e.g., ERA5) provide data only up to around 1 hPa. To apply nudging above this limit, reanalysis fields must be extrapolated to the model's upper levels—a procedure prone to substantial uncertainties and interpolation errors. These errors can degrade model performance; for example, Zhang et al. (2022b) demonstrated that numerical interpolation errors in reanalysis data used for nudging can introduce spurious cloud radiative effects, thereby compromising the physical realism of nudged simulations. To mitigate these issues, we introduce the threshold parameter P_0, above which a linear relaxation is applied to gradually reduce the nudging tendency. Specifically, for model levels with pressure $P_m < P_0$, the nudging tendency is scaled down linearly to zero as the pressure approaches the model top. This formulation ensures that nudging is smoothly deactivated in the uppermost layers where reanalysis information is unreliable or unavailable, thereby avoiding the introduction of artificial signals into the model dynamics. In addition, as shown in Table 2, we specify different values of P_0 for different nudging variables, following guidance from the nudging implementation in the GFDL FV3 model (NOAA GFDL, 2020), which was found to be effective based on results in our study. While a comprehensive sensitivity analysis of the selected P_0 values was beyond the scope of this study, the configuration was informed by established practices and demonstrated robust performance in our simulations.

Second, near-surface nudging presents challenges due to the strong influence of local processes and topographic variability. The third term in Eq. (3) mitigates these issues by modulating the nudging tendency within the planetary boundary layer (PBL) through a hyperbolic tangent function of the model-simulated geopotential height Z_m and the PBL height Z_b. This formulation effectively reduces nudging when $Z_m < Z_b$, preserving the development of mesoscale structures and preventing artificial suppression of subgrid variability. This approach is informed by earlier studies (e.g., Lo et al., 2008; Vincent and Hahmann, 2015), which found that strong nudging in the boundary layer can overly constrain the model to large-scale forcing, increasing biases and dampening realistic variability. Furthermore, mismatches in surface elevation between reanalysis and Earth system models exacerbate interpolation errors in near-surface levels, further justifying reduced nudging in these regions.

https://doi.org/10.5194/egusphere-2025-4277
Preprint. Discussion started: 21 October 2025

As further elaborated in Section 4, the modifications in Eq. (3) enhance the robustness and physical realism of nudged EAMv2 simulations.

2.3 Model Simulations

In this study, we conducted simulations with EAMv2 following the Atmospheric Model Intercomparison Project (AMIP) protocol (Gates et al., 1999). This setup couples the interactive atmosphere and land components of EAMv2 with prescribed monthly sea surface temperature (SST) and sea ice extent derived from observational data. The SST and sea ice boundary conditions were sourced from the input4MIPs datasets (Reynolds et al., 2002), ensuring consistency with the AMIP framework. To incorporate external forcings, we prescribed data for volcanic aerosols, solar variability, greenhouse gas concentrations, and anthropogenic emissions of aerosols and their precursors, following the protocols established by the World Climate Research Programme's Coupled Model Intercomparison Project Phase 6 (CMIP6) (Eyring et al., 2016; Hoesly et al., 2018; Feng et al., 2020). For anthropogenic aerosol emissions and precursor gases, present-day conditions were represented using 2010 data.

Three groups of simulations are presented in this study (see Table 1). The first group includes two free-running baseline simulations. The first simulation, referred to as CTRL, is a short-term run spanning from October 2009 to February 2010. The second simulation, referred to as CLIM, is a long-term run covering the period from 1 January 2007 to 31 December 2017. These two simulations serve as the baseline for the nudging experiments conducted in this study. The CLIM simulation specifically spans 2007–2017, as ERA5 reanalysis data were only processed for this time period.

Table 1. List of simulations and key nudging setups in this study. Nudging was applied at each physics time step (30 min). A linear interpolation was used to map the 3-hourly ERA5 atmospheric (three-dimensional) and land surface (single-level) data to each model step to compute the nudging tendency. All simulations in this table use present-day (PD, year 2010) external forcing for anthropogenic aerosol and precursor emissions, consistent with the EAMv2 atmosphere-only setup (Golaz et al., 2022). *Note:* In NDG-UVTQ_SRF1, U, V, T, and Q were nudged as in NDG-UVTQ, with additional constraints on near-surface variables (U10, V10, T2, TD2, TS). Here, U10 and V10 are the horizontal wind components at the 10 m reference level from ERA5. They are used to nudge the wind fields in the lowest EAMv2 model layer, which is approximately centered at 10m.

Group	Simulation name	Atmosphere	Land surface	Period	Nudging
1	CTRL	None	None	Oct 2009 – Feb 2010	None
1	CLIM	None	None	Jan 2007 – Dec 2017	None
2	DNDG-UV	U, V, T	None	Oct 2009 – Feb 2010	Eq. (2)
2	DNDG-UVT	U, V, T	None	Oct 2009 – Feb 2010	Eq. (2)
2	DNDG-UVQ	U, V, T	None	Oct 2009 – Feb 2010	Eq. (2)
2	DNDG-UVTQ	U, V, T, Q	None	Oct 2009 – Feb 2010	Eq. (2)
2	RNDG-UVTQ	U, V, T, Q	None	Oct 2009 – Feb 2010	Eq. (3)
3	NDG-UV	U, V	None	Jan 2007 – Dec 2017	Eq. (3)
3	NDG-UVT	U, V, T	None	Jan 2007 – Dec 2017	Eq. (3)
3	NDG-UVTQ	U, V, T, Q	None	Jan 2007 – Dec 2017	Eq. (3)
3	NDG-UVTQ_SRF1	U, V, T, Q	U10, V10, T2, TD2, TS	Jan 2007 – Dec 2017	Eq. (3)

https://doi.org/10.5194/egusphere-2025-4277
Preprint. Discussion started: 21 October 2025

The second group comprises a series of short-term nudged EAMv2 simulations conducted over the same period as CTRL, in which the atmospheric model state is constrained toward the ERA5 reanalysis. A detailed workflow of the EAMv2 nudging framework is provided in Figure 1b of Zhang et al. (2022a). Briefly, the nudging tendency terms $\dot{\boldsymbol{R}}$ are computed by comparing the model's prognostic variables, saved immediately before the radiation parameterization step, with the corresponding ERA5 fields. These tendency terms are then applied after the physics parameterization suite to adjust the model state variables accordingly. The simulations labeled "DNDG" in Group 2 using the "default nudging scheme" were conducted using Eq.(2) to compute $\dot{\boldsymbol{R}}$, by constraining the EAMv2 model states toward different subsets of the ERA5 reanalysis fields:

- horizontal winds only (labeled DNDG-UV"),
- horizontal winds and temperature (labeled DNDG-UVQ"),
- horizontal winds and temperature (labeled DNDG-UVT"), and
- horizontal winds, temperature, and humidity (labeled "DNDG-UVTQ").

These simulations were used to demonstrate the limitations associated with humidity nudging using Eq.(2). An additional simulation, referred to as RNDG-UVTQ, was performed using the same nudging configuration as DNDG-UVTQ but employed the revised nudging formulation in Eq.(3), which is proposed in this study to improve model performance when nudging humidity. The tunable parameters P_0 and Z_b used in Eq.(3) were assigned the values listed in Table2. These values were determined based on a series of short-term nudged EAMv2 simulations (not shown), although further tuning may be necessary when applying this formulation with different reanalysis products. A detailed comparison of RNDG-UVTQ with other experiments in Group 2 will be presented in Section 3, where we demonstrate the effectiveness of the revised nudging formulation of Eq. (3) in better addressing the humidity nudging in EAMv2 simulations.

Table 2. Choices on threshold parameters used in Eq. (3) for nudged EAMv2 simulations in this study.

Variable	U	V	T	Q
P_0 (Pa)	3000	3000	1000	10000
Z_b	PBLH	PBLH	PBLH	PBLH

The third group consists of long-term nudged EAMv2 simulations conducted over the same period as CLIM, using the revised nudging formulation described in Eq.(3). To assess the impact of different nudging configurations on the model's long-term simulation fidelity, three simulations were performed by nudging subsets of the ERA5 reanalysis fields: horizontal winds only (NDG-UV), winds and temperature (NDG-UVT), and winds, temperature, and humidity (NDG-UVTQ). These experiments were designed to evaluate whether nudging improves the agreement between EAMv2 simulations and the ERA5 reanalysis on climatological timescales. An additional simulation, labeled NDG-UVTQ_SRF1, extended the NDG-UVTQ configuration by also nudging U, V, T, and Q fields at the model's lowest vertical level, thereby directly constraining land–atmosphere

https://doi.org/10.5194/egusphere-2025-4277
Preprint. Discussion started: 21 October 2025

interactions. This modification introduces surface-level nudging tendencies derived from ERA5 and is intended to better represent surface processes in the model. As discussed in Section 4, incorporating these surface constraints enhances the model's skill in simulating land-surface variables and precipitation.

It is important to note that all nudged EAMv2 simulations listed in Table 1 differ only in their choice of nudged variables; other aspects of the nudging configuration follow recommendations from prior studies (Sun et al., 2019; Zhang et al., 2022a). The ERA5 atmospheric and land surface reanalysis fields were originally produced on a 0.25° × 0.25° horizontal grid with 37 pressure levels. These data were remapped to the EAMv2 model grid, using the "pg2" horizontal grid and 72 hybrid sigma-pressure levels, and subsequently employed as reference fields for the nudging simulations. The remapping procedures (both horizontal and vertical) followed the algorithms proposed for nudging in the Community Earth System Model Version 2 (CESM2) (CESM2, 2025). Furthermore, linear-function nudging was applied to the 3-hourly ERA5 reanalysis to derive nudging tendencies at each model time step (i.e., every 30 minutes). The nudging relaxation time scale τ in Eq. (3) was set to 6 hours for the upper atmospheric layers and 1 hour for the land surface layer. These parameters were empirically chosen and are shown to perform well based on the evaluation results presented in the following sections.

3 Sensitivity Experiments for Nudging Strategies

As a first step, we compared the strength of the two nudging formulations specified in Eq.(2) and Eq.(3), with a particular focus on cases where humidity is included as a nudged variable. This investigation was motivated by the findings of Sun et al. (2019), who reported that humidity nudging using Eq. (2) caused substantial disruptions to the hydrological cycle, as evidenced by a significant reduction in precipitation in simulations with an earlier version of the E3SM atmosphere model (EAMv1; see their Figures 6 and 7). Our analysis focuses on a series of short-term EAMv2 simulations described in Table 1 (CTRL and Group 2). These short simulations were intended to reduce computational cost; nevertheless, the limited simulation length does not affect the main conclusions drawn in this section.

Figure 1 presents Hovmöller diagrams of the daily precipitation rate (PRECT; units: mm day^{-1}) over the tropics for the period December 2009 to February 2010. Consistent with the findings of Sun et al. (2019), nudging large-scale winds (U, V) and temperature (T) toward ERA5 reanalysis (DNDG-UV and DNDG-UVT; panels c–d) using Eq.(2) substantially improves agreement between EAMv2 simulations and TRMM observations (panel a), relative to the free-running simulation (CTRL; panel b). This improvement is reflected in systematic increases in pattern correlation coefficients (PCC) and reductions in root-mean-square errors (RMSE) compared to the CTRL baseline. Incremental gains from DNDG-UV to DNDG-UVT further underscore the added value of temperature nudging. In contrast, substituting temperature with humidity (DNDG-UVQ; panel e) results in a noticeable suppression of precipitation intensity, despite improved spatial correlation. This degradation becomes more pronounced when both temperature and humidity are nudged alongside winds (DNDG-UVTQ; panel f), revealing a key trade-off in the traditional nudging formulation: nudging Q improves the location and timing of precipitation (higher PCC) but substantially worsens its magnitude relative to observations (higher RMSE). These adverse effects are effectively mitigated by the revised nudging formulation proposed in this study (Eq.3). The RNDG-UVTQ simulation (panel g) retains the enhanced

https://doi.org/10.5194/egusphere-2025-4277
Preprint. Discussion started: 21 October 2025

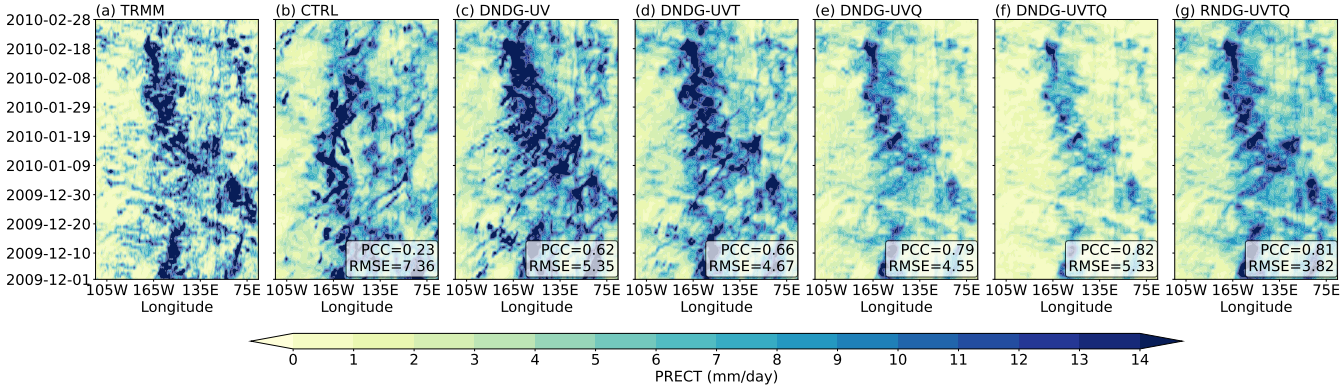

Figure 1. Zonal-mean Hovmöller diagrams of daily precipitation rate (mm day^{-1}) over the tropics region (10°S–10°N, 60°E–90°W), based on TRMM observations (panel a), the free-running EAMv2 simulation (CTRL; panel b), and nudged EAMv2 simulations (panels c–g) labeled as "DNDG" or "RNDG". Simulations labeled "DNDG" use the nudging formulation in Eq. (2), while "RNDG" simulations apply the revised formulation in Eq. (3). The suffixes UV, UVT, and UVTQ denote the subsets of model state variables nudged toward the ERA5 reanalysis: large-scale winds (U, V), temperature (T), and humidity (Q), respectively. Pattern correlation coefficients (PCC) and root-mean-square errors (RMSE) between each EAMv2 simulation (panels b–g) and the TRMM observations (panel a) are reported in the bottom-right corner of each panel. Further details on the simulation setups are provided in Section 2.3 and Table 1.

spatial structure achieved by DNDG-UVTQ (high PCC) while avoiding the associated increase in RMSE, thereby achieving comprehensive improvement without the trade-offs observed in the default nudging approach. Compared to DNDG-UV (panel c) and DNDG-UVT (panel d), RNDG-UVTQ further improves hindcast skill over the tropics, as indicated by both higher PCC and lower RMSE. Similar improvements are found in other regions, including the Northern Hemisphere midlatitudes (figures not shown).

Figure 2 presents the global pattern correlation coefficients (PCCs) and normalized root-mean-square errors (RMSEs) for selected physical variables, computed by comparing EAMv2 simulations against the observational datasets listed in Table B1, averaged over the three months from December 2009 to February 2010. RMSEs are normalized by the observed RMS values to enable consistent comparison of relative errors across variables with differing units and magnitudes. Overall, the EAMv2 simulations reproduce large-scale spatial patterns reasonably well, with PCCs exceeding 0.9 for most variables (Fig.2a). However, simulations using the default nudging formulation in Eq.(2), particularly when both temperature and humidity are constrained (DNDG-UVTQ, cyan bars), exhibit degraded pattern correlation for cloud radiative effects (SWCF and LWCF), precipitation (PRECT), and sensible heat fluxes (SHFLX), relative to the free-running control simulation (CTRL, grey bars). These deficiencies are largely mitigated in the RNDG-UVTQ simulation (red bars), highlighting the effectiveness of the revised nudging strategy. In terms of RMSEs (Fig.2b), nudging generally reduces errors in directly constrained state variables such as surface pressure (PSL), 2-meter air temperature (TREFHT), and 500 hPa geopotential height (Z500). However, simulations that include humidity nudging using the default formulation (DNDG-UVQ and DNDG-UVTQ) show substantial increases in RMSE for

https://doi.org/10.5194/egusphere-2025-4277
Preprint. Discussion started: 21 October 2025

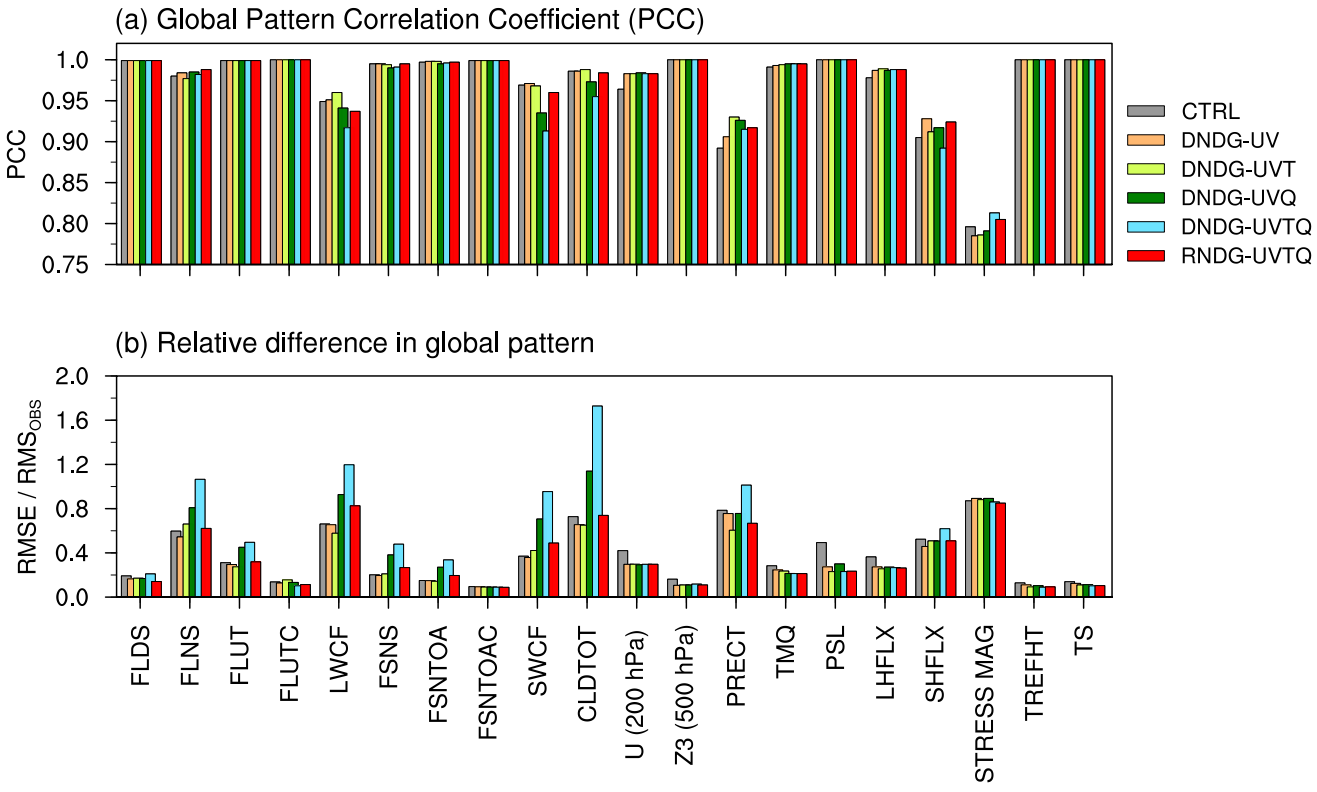

Figure 2. Comparison of global pattern correlation coefficients (PCC; Panel a) and normalized root-mean-square errors (RMSE; Panel b) from EAMv2 free-running and nudged simulations, averaged over the 3 months from December 2009 to February 2010. The physical variables along the x-axis are listed in Table B1 in the Appendix B. The normalized RMSE is computed as the root-mean-square differences between the model and the corresponding observational dataset (Table B1), divided by the root-mean-square of the observed field ($\mathrm{RMS_{OBS}}$), providing a dimensionless measure of relative error magnitude. Different colors represent distinct nudging configurations, which vary in the frequency of the constraining data and the ordering of the applied physical tendencies. All statistics are computed relative to the observational datasets listed in Table B1. Additional discussion is provided in Section 3 and Appendix B, and details of the simulation setups are given in Section 2.3 and Table 1.

https://doi.org/10.5194/egusphere-2025-4277
Preprint. Discussion started: 21 October 2025

precipitation, total cloud fraction (CLDTOT), and cloud-related radiative fluxes (FLNS, LWCF, and SWCF), suggesting that over-constraining thermodynamic fields can disrupt the model's physical consistency. While the revised formulation in Eq.(3), as implemented in RNDG-UVTQ, effectively alleviates these issues, it still shows some degradation in RMSEs for cloud and radiation fields relative to CTRL. As discussed further in Section 3.3, these residual errors may stem from the absence of nudging over land and from compensating errors in the model system. Nevertheless, the comparison between RNDG-UVTQ and DNDG-UVTQ demonstrates that the proposed nudging strategy significantly improves hindcast performance in EAMv2 by addressing key limitations of the default humidity nudging approach.

4 Improving the hindcast skills of simulations nudged to reanalysis

In this section, we assess the performance of the present-day long-term simulations in Group 3 of Table 1, which were conducted using the revised nudging formulation described in Eq. (3) and implemented with various nudging strategies. Emphasis is placed on evaluating the fidelity of these nudged EAMv2 simulations in reproducing key observed physical and dynamical fields, based on their hindcast skill.

4.1 Model Biases in Large-Scale Mean Environmental Conditions

Figure 3 presents the zonal and annual mean biases in zonal wind (U), temperature (T), and specific humidity (Q) from the CLIM simulation (first column) and the nudged EAMv2 experiments. All biases are computed relative to ERA5 reanalysis and averaged over the 2008–2017 period. Dotted regions indicate statistically significant differences at the 95% confidence level based on a Student's t-test. Biases over regions of high topography are masked due to large extrapolation errors.

Consistent with previous studies (Sun et al., 2019; Zhang et al., 2022a), wind-only nudging in the NDG-UV simulation substantially reduces model biases in the zonal wind field (U; Fig.3a1–a2). Although hemispheric cancellation obscures coherent patterns in the zonal mean of meridional wind (V), NDG-UV effectively suppresses the dominant error centers present in the CLIM simulation, particularly in the upper troposphere (Fig.3b1–b2). Its impact on correcting temperature (T) and specific humidity (Q) biases, however, remains limited (Fig.3c1–c2, d1–d2). Extending nudging to include temperature (NDG-UVT) leads to a marked reduction in temperature biases while retaining the wind improvements (Fig.3a3–c3), but this configuration introduces undesirable increases in humidity biases, especially in the tropical and subtropical middle troposphere (Fig.3d3). These spurious responses are effectively eliminated when humidity nudging is also applied (NDG-UVTQ), as shown in Fig.3d4, underscoring the importance of jointly constraining both temperature and humidity to achieve realistic thermodynamic conditions in hindcast simulations. Among all tested configurations, NDG-UVTQ yields the most substantial reduction in biases across the majority of dynamical (U, V) and thermodynamical (T, Q) fields (Fig. 3a4–d4), resulting in a more accurate representation of large-scale atmospheric states across most regions of the globe. One notable exception is the tropical lower troposphere (1000–800 hPa), where increased biases emerge, possibly due to over-constraining by the nudging scheme. Comparable improvements are also observed in the NDG-UVTQ_SRF1 strategy, which incorporates additional nudging of U, V, T, and Q near the surface (figure not shown).

https://doi.org/10.5194/egusphere-2025-4277
Preprint. Discussion started: 21 October 2025

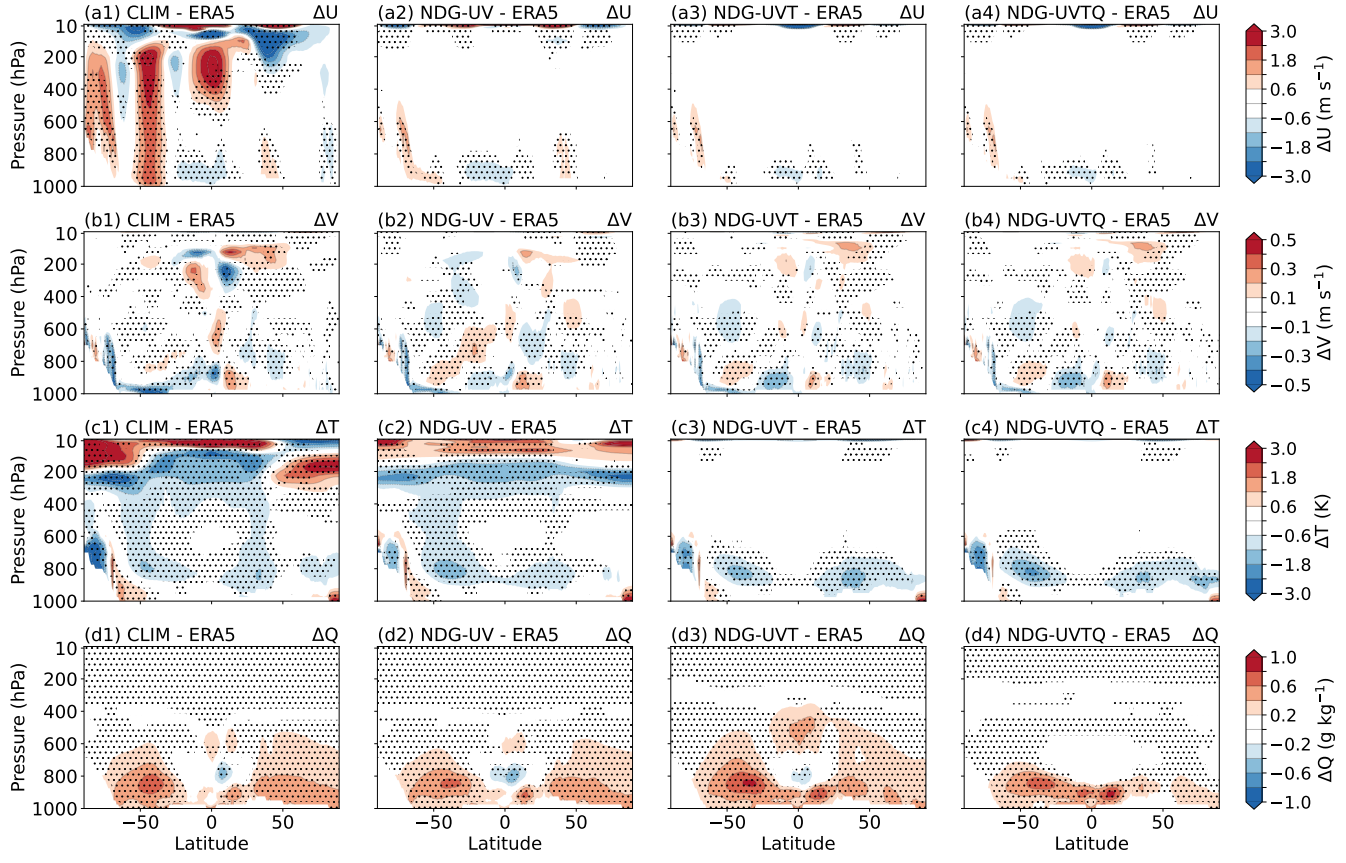

Figure 3. Zonal and annual mean model biases in zonal wind (U, unit: m s^{-1}, panels a1–a4), meridional wind (V, unit: m s^{-1}, panels b1-b4), temperature (T, unit: K, panels c1–c4), and water vapor mixing ratio (Q, unit: g kg^{-1}, panels d1–d4) averaged from 2008 to 2017 from free-running (i.e., CLIM, first column), UV-nudging (NDG-UV, second column), UVT-nudging (NDG-UVT, third column) and UVTQ-nudging (NDG-UVTQ, fourth column) EAMv2 simulations. The biases are derived by comparing monthly mean EAMv2 simulations with ERA5 reanalysis. The dotted region indicates the differences are significant at a 95% confidence level from a Student's t-test. The log-linear interpolation is used to regrid the EAMv2 data on the hybrid sigma-pressure level to the pressure level for comparison with the ERA5 reanalysis. Details of the simulation setups can be found in Table 1.

https://doi.org/10.5194/egusphere-2025-4277
Preprint. Discussion started: 21 October 2025

A more quantitative assessment of hindcast performance is presented in Fig. 4, using root-mean-square error (RMSE) and anomaly correlation coefficient (ACC) metrics derived from comparisons with observational and reanalysis datasets (see Table B1). Figure 4 displays heatmaps of RMSE values for selected upper-atmosphere (panel a) and surface-level (panel b) variables, normalized by the multi-experiment mean RMSE for each variable. Values near one indicate average model skill; values greater than one (purple shading) denote larger errors, while values below one (green shading) indicate improved agreement with observations. All nudged simulations outperform the free-running CLIM case, exhibiting systematic RMSE reductions across both atmospheric levels. The best performance is observed in the two nudged simulations (i.e., NDG-UVTQ and NDG-UVTQ_SRF1), in which all major prognostic variables are nudged (Fig. 4a). Compared to NDG-UVTQ, the inclusion of land-surface nudging in NDG-UVTQ_SRF1 further improves fidelity in near-surface temperature (T2M, TS) and total column moisture (TPW; Fig. 4b), although it introduces a slight degradation in the simulation of shortwave radiative fluxes (e.g., FSNT, FSNS, FSNSC) and cloud-related quantities (e.g., LWP, IWP). The behavior of the NDG-UVTQ and NDG-UVTQ_SRF1 configurations will be examined in more detail in the following subsections. Despite these trade-offs, both simulations maintain strong agreement with large-scale atmospheric patterns, as evidenced by high ACC values (Fig. C1), consistent with previous findings (Sun et al., 2019; Zhang et al., 2022a).

Overall, the results presented in this section demonstrate that incorporating humidity nudging—especially when implemented within a revised multi-variable nudging framework—significantly enhances the hindcast skill of EAMv2. These improvements span both dynamical and thermodynamical aspects of the simulation. Crucially, simultaneous nudging of temperature and humidity is not only effective in reducing biases but also essential for maintaining consistency in energy and mass budgets. This need partly arises from the default nudging formulation of Eq. (2), which applies independent relaxation timescales to each nudged variable without accounting for their physical covariances. When only temperature is nudged (as in NDG-UVT), such unbalanced constraints can disrupt cross-variable relationships and generate spurious responses—particularly in humidity fields.

4.2 Hindcast Skills of Precipitation and Land-atmosphere Interaction

Figure 5 presents Hovmöller diagrams of daily precipitation rate (PRECT; units: mm day^{-1}) for the year 2011 over selected tropical (panels a1–e1) and midlatitude regions (panels a2–e2), comparing the free-running and nudged simulations listed in Table 1. We can see that NDG-UVTQ in this study successfully preserves both the spatial structure and magnitude of precipitation in the tropics (panels a1–e1) and midlatitudes (panels a2–e2) throughout the year. Notably, NDG-UVTQ further enhances precipitation hindcast skill in the tropics relative to NDG-UV and NDG-UVT, as evidenced by higher pattern correlation coefficients (PCCs) and lower root-mean-square errors (RMSEs). In the midlatitude regions (mid-lat, panels a2–e2), substantial improvements in precipitation hindcast skill are already evident with wind-only nudging (NDG-UV) compared to the free-running CLIM simulation, highlighting the dominant role of large-scale circulation in driving midlatitude precipitation. While further nudging of temperature and humidity (NDG-UVT and NDG-UVTQ) leads to modest additional reductions in RMSE, the differences between NDG-UVT and NDG-UVTQ in other precipitation-related fields (Fig 4) highlight important distinctions between the two nudging strategies.

https://doi.org/10.5194/egusphere-2025-4277
Preprint. Discussion started: 21 October 2025

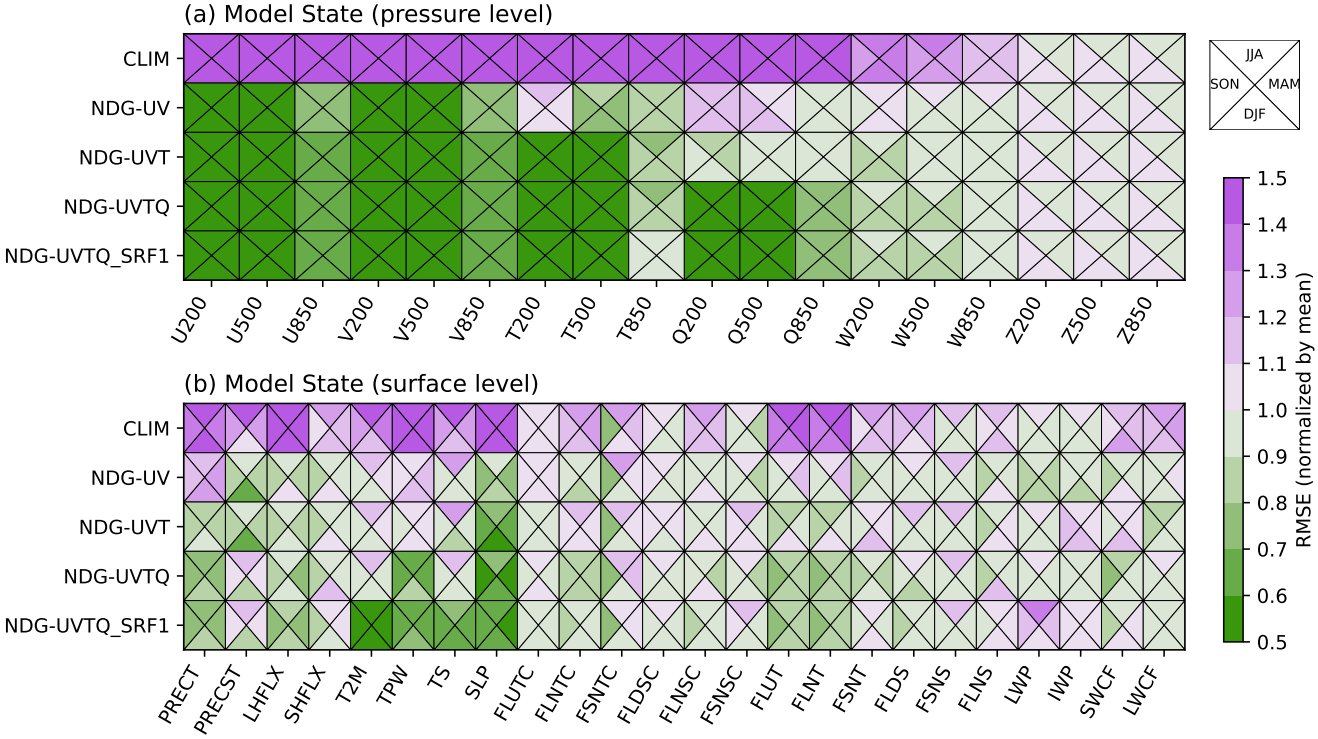

Figure 4. Heatmap showing normalized root-mean-square errors (RMSE) of 10-year average seasonal mean physical quantities from EAMv2 free-running (CLIM) and nudged simulations (NDG-UV, NDG-UVT, NDG-UVTQ, NDG-UVTQ_SRF1) in Table 1. The top panel (a) shows upper-atmosphere variables on selected pressure levels calculated from 6-hourly model output, while the bottom panel (b) shows surface-level variables computed from monthly mean model output. Each square is subdivided into four triangles representing seasonal mean values for austral summer (DJF), autumn (MAM), winter (JJA), and spring (SON), respectively. Colors indicate the magnitude of RMSE, normalized by the multi-model mean across experiments for each variable (row-wise). Experiments are listed along the y-axis and variables along the x-axis. Definitions of the physical quantities and the corresponding reference datasets used for RMSE calculation are provided in Table B1.

https://doi.org/10.5194/egusphere-2025-4277
Preprint. Discussion started: 21 October 2025

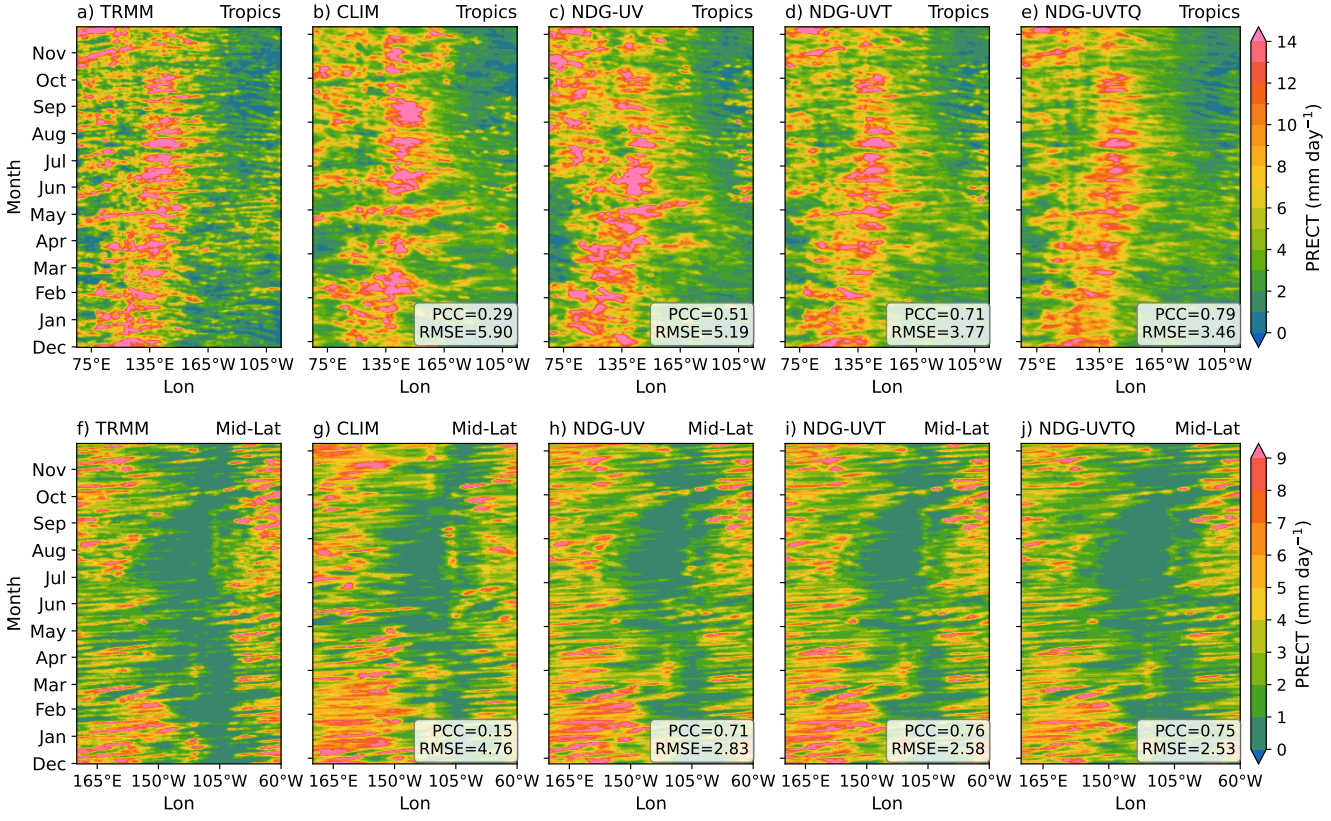

Figure 5. Evaluation of the spatiotemporal distribution of daily precipitation from 1 December 2010 to November 30 2011 over the tropics (10°S–10°N, 60°E–90°W; upper row) and Northern Hemisphere midlatitude region (25°N–50°N, 150°E–60°W; lower row). Panels (a, f): Hovmöller diagrams of meridionally averaged total precipitation rates (PRECT, mm day^{-1}) from TRMM satellite observations. Panels (b, g): CLIM simulation. Panels (c–e, h–j): simulations with wind-only nudging (NDG-UV), wind-plus-temperature nudging (NDG-UVT), and full-variable nudging (NDG-UVTQ), respectively. Top labels indicate correlation (Corr.) and RMSE with respect to TRMM. Simulation setups are described in Section 2.3 and Table 1.

https://doi.org/10.5194/egusphere-2025-4277
Preprint. Discussion started: 21 October 2025

Figure 6 presents mean biases in total precipitable water (TPW; first row), outgoing longwave radiation (FLUT; second row), precipitation rate (PRECT; third row), and surface air temperature (T2M; fourth row) from EAMv2 simulations compared against observations. Relative to the free-running CLIM simulation, the NDG-UVT case exhibits a spurious increase in TPW across many regions, particularly within the midlatitude storm track zones (panels a1–a2). This artificial moistening of atmospheric columns coincides with an enhanced underestimation of FLUT (panels b1–b2) in the same regions. While constraining the temperature field improves long-term mean precipitation (panels c1–c2), the simulation struggles to maintain realistic atmospheric mass and energy balances—an issue previously reported by Zhang et al. (2022b). When additional humidity nudging is applied (NDG-UVTQ), the spurious TPW increase is effectively removed, leading to a substantial global reduction in TPW biases (panel a3). This demonstrates that jointly constraining temperature and specific humidity is essential for maintaining a realistic moisture distribution and improving the representation of precipitation. Nevertheless, NDG-UVTQ tends to over-correct FLUT, resulting in overestimated outgoing longwave radiation in many regions relative to both NDG-UVT and CLIM (panel b3). It also leads to a systematic weakening of long-term mean precipitation over midlatitude regions. This apparent inconsistency with the improved synoptic-scale performance shown in Fig. 5e2 arises from differences in spatial and temporal scales across the diagnostics.

One key factor contributing to the unfavorable FLUT and PRECT biases in NDG-UVTQ is the lack of constraints on the land surface model state. As shown in panels d1–d3, surface air temperature (T2M) biases remain largely unchanged in both magnitude and spatial distribution, regardless of whether a subset or all of the upper-atmosphere variables (U, V, T, Q) are nudged. This suggests that upper-air nudging alone is insufficient to effectively influence surface conditions, underscoring the importance of incorporating surface or land-model constraints to better maintain the model's consistency with observed surface water and energy fluxes. As demonstrated in panels a4–d4, the NDG-UVTQ_SRF1 experiment, which extends nudging to include the land surface layer, yields substantial reductions in surface biases such as T2M (panel d4). Moreover, NDG-UVTQ_SRF1 restores FLUT closer to the model's favorable climatology (panel b4 versus b1) while also mitigating the excessive weakening of midlatitude precipitation evident in NDG-UVTQ (panel c4 versus c1).

Furthermore, the biases in large-scale moisture convergence (LSMC; Figure C3) in NDG-UVT, NDG-UVTQ and NDG-UVTQ_SRF1 do not show the corresponding changes in total precipitable water (TPW; panels a2–a4) or precipitation (PRECT; panels c2–c4). This lack of a coherent response between LSMC and TPW suggests that the sensitivity of precipitation to nudging strategies does not arise from changes in large-scale moisture transport, but rather from differences in microphysical quantities triggered by the nudging configurations. This hypothesis is further supported by the strong sensitivity of cloud properties and the consistent changes observed in both shortwave and longwave cloud radiative effects across the 10-year simulations (Fig. C2). Importantly, these unfavorable responses in cloud-related quantities should not be interpreted as a degradation in hindcast skill resulting from temperature and humidity nudging. Instead, they likely reflect that the microphysics parameterizations were originally tuned to the biased atmospheric state of the free-running model (i.e., CLIM), rather than to the more realistic conditions achieved in the nudged EAMv2 simulations. Some retuning is therefore expected to be necessary to ensure optimal performance of the microphysics schemes under nudged configurations, although such adjustments lie beyond the scope of this study.

https://doi.org/10.5194/egusphere-2025-4277
Preprint. Discussion started: 21 October 2025

Taken together with the findings from the previous section, our results in this section support the conclusion that simultaneous nudging of all major model state variables, including winds, temperature, and humidity, is essential not only for enhancing the model's hindcast skill in reproducing the real atmosphere but also for maintaining realistic mass and energy budgets. Furthermore, nudging the land-surface layer contributes to improved physical realism in long-term simulations of the water and energy budgets. Intercomparison across nudging configurations indicates that microphysical processes and associated cloud properties in EAMv2 are sensitive to land surface conditions and land–atmosphere interactions, which in turn influence the fidelity of long-term water and energy budgets.

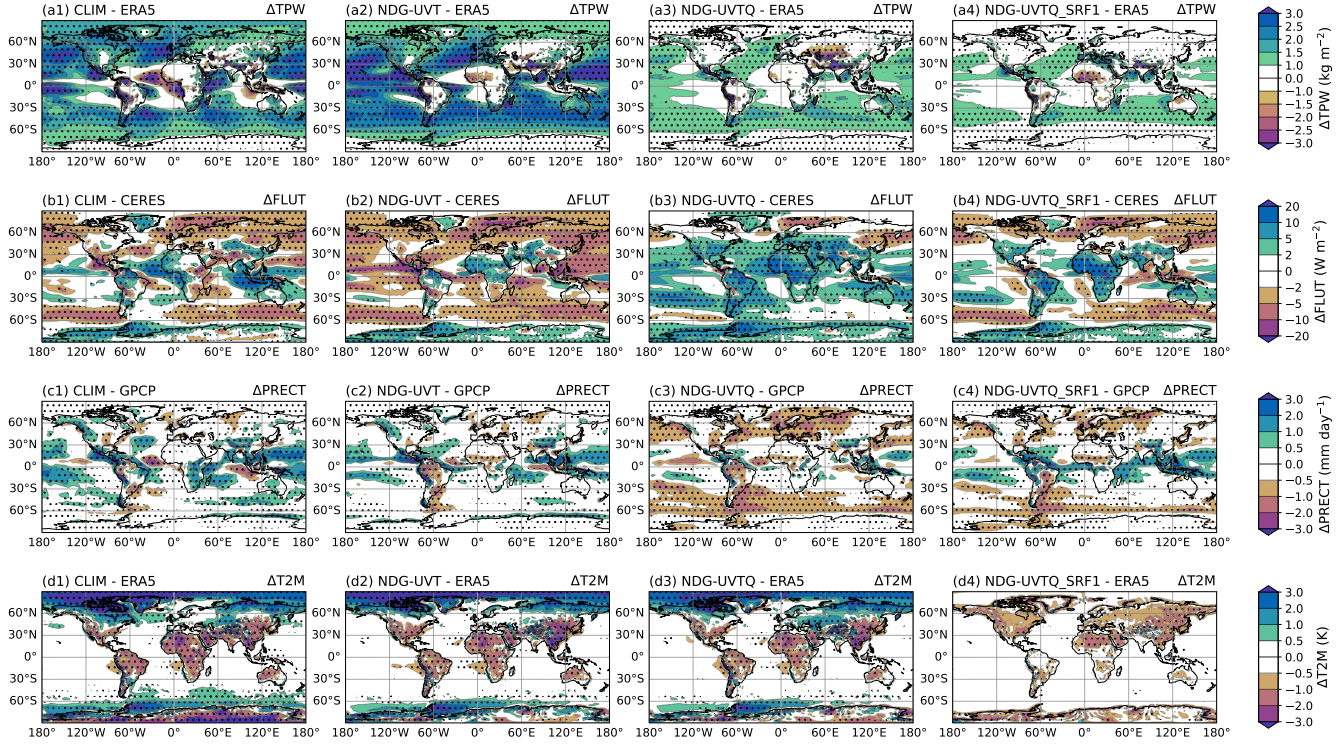

Figure 6. Horizontal distribution of annual mean model biases in total precipitable water (TPW, unit: kg m^{-2}; panels a1–a4), outgoing longwave radiation (FLUT, unit: W m^{-2}; panels b1–b4), surface air temperature (T2M, unit: K; panels b1–b3), and total precipitation rate (PRECT, unit: mm day^{-1}; panels a1–a3), averaged over 10 simulation period from 2008 to 2017. Results are shown for CLIM (first column), NDG-UVT(second column), NDG-UVTQ (third column), and NDG-UVTQ_SRF1 (fourth column). Biases are computed relative to observations/reanalysis from GPCP (PRECT; Adler et al., 2003), ERA5 (TREFHT, TMQ; Hersbach et al., 2020), and CERES-EBAF (FLUT; Kato et al., 2018). Dotted regions indicate statistically significant differences at the 95% level based on a Student's *t*-test. See Table 1 for simulation details.

https://doi.org/10.5194/egusphere-2025-4277
Preprint. Discussion started: 21 October 2025

5 Implication on High-impact Weather Assessment with EAM

As mentioned in Section 1, nudging techniques have been applied in model intercomparison projects such as ExtremeX, which focus on weather and long-term environmental extremes. This motivates an evaluation of whether the humidity nudging strategy proposed in this study can enhance model performance for such applications. In this section, we compare the EAMv2 free-running simulation (CLIM) with three nudged simulations (NDG-UV, NDG-UVT, and NDG-UVTQ_SRF1) to assess the effectiveness of the proposed nudging strategies in improving EAMv2's representation of high-impact weather systems and to explore their implications for evaluating such events using low-resolution models.

We begin our discussion with tropical cyclones (TCs), as they represent a relevant and challenging example. Low-resolution models like EAMv2, which operate at approximately 1-degree horizontal resolution, are not expected to fully resolve TCs. Therefore, dynamical or statistical downscaling is often required to assess TC characteristics in such models. In these cases, accurate simulation of large-scale environmental conditions becomes critical for enabling meaningful TC assessments. Figure 7 shows the TC track densities obtained using the TempestExtremes package (Ullrich et al., 2021), applied to 6-hourly mean sea level pressure (PSL) data from the ERA5 reanalysis and the EAMv2 simulations listed in Table 1. The tracking algorithm and configuration follow the methodology described in Zhang et al. (2024) (see their Appendix A3 for details). The ERA5-based track density serves as the observational reference, providing a benchmark for evaluating the realism of TC activity simulated in the various model experiments. All datasets were regridded to a 1° latitude–longitude grid before TC tracking to ensure a consistent and fair comparison. Although the original ERA5 data has a native resolution of 0.25°, its interpolation to 1° retains much of the fine-scale information relevant to TC structures. It is not surprising that all EAMv2 simulations, including those with atmospheric nudging (Fig. 7b through e), systematically underestimate TC occurrence frequency compared to ERA5 (Fig. 7a) across all basins. This underestimation is largely attributed to the coarse horizontal resolution of EAMv2, which limits the model's ability to resolve the smaller-scale dynamical features critical for TC development and maintenance. However, a comparison between nudged and free-running (CLIM) simulations reveals notable differences in the representation of TC-related weather systems, owing to improved constraints on the large-scale circulation in nudged configurations. Specifically, the CLIM simulation (Fig. 7b) shows reasonably good agreement with ERA5 in terms of the spatial pattern of TC track density over the Pacific and Indian Ocean basins but significantly underestimates TC occurrence over the northeastern Pacific and North Atlantic. In contrast, all nudged simulations exhibit higher pattern correlation coefficients (PCCs) with ERA5 and show a marked reduction in the underestimation over the Pacific and Indian Ocean regions (Fig. 7c–e), indicating that nudging improves the representation of TC-associated weather-scale systems to the extent permitted by the low-resolution EAMv2. In addition, the NDG-UVT and NDG-UVTQ_SRF1 experiments (Fig. 7d–e) do not show significant differences from NDG-UV (Fig. 7c), suggesting that the ability of low-resolution EAMv2 to capture TC-related features is primarily constrained by its dynamical fidelity rather than by additional nudging of thermodynamic fields such as temperature and humidity.

The differences observed in Fig. 7 among the EAMv2 simulations, with and without nudging and under varying degrees of thermodynamic constraint, can be better understood by examining the associated large-scale environmental conditions that influence tropical cyclone (TC) activity. Figure 8 presents the Genesis Potential Index (GPI) along with its key contributing

https://doi.org/10.5194/egusphere-2025-4277
Preprint. Discussion started: 21 October 2025

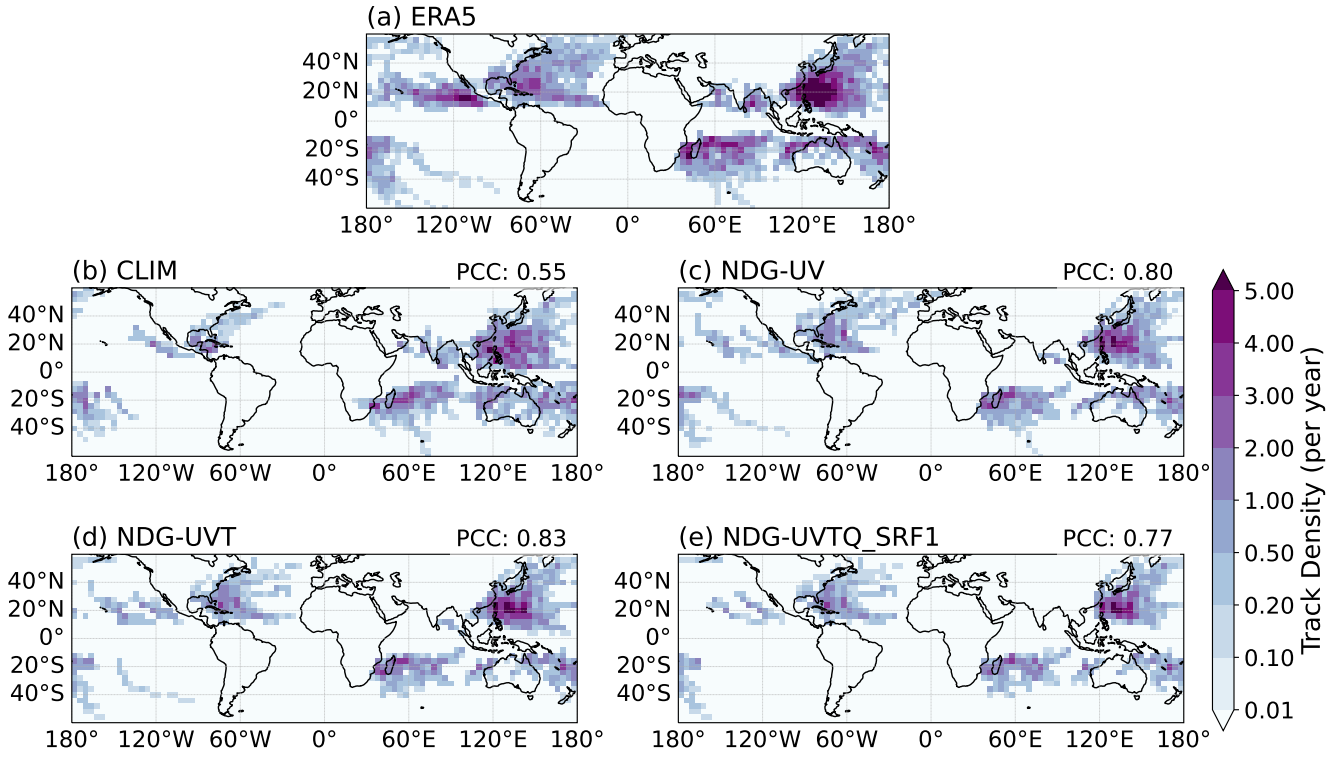

Figure 7. Tropical cyclone (TC) track densities computed from the ERA5 reanalysis dataset (panel a), the EAMv2 free-running simulation (CLIM; panel b), and nudged simulations including NDG-UV (panel c), NDG-UVT (panel d), NDG-UVTQ (panel e), and NDG-UVTQ_SRF1 (panel f), over the period 2008–2017. All metrics are calculated on a $4^\circ \times 4^\circ$ latitude–longitude grid. Track density is defined as the number of 6-hourly TC positions occurring within each grid cell per year, providing a measure of TC transit frequency. Cyclones were identified using the TempestExtremes algorithm (Ullrich et al., 2021), applied to 6-hourly sea-level pressure (PSL), 10-meter wind, and surface geopotential height fields. Detection begins with locating local PSL minima enclosed by closed contours with Laplacian magnitude $\geq$ 200 Pa and contour radius $\leq 5.5^\circ$. A fallback method identifies vortex candidates based on a warm core anomaly, computed from the difference between 200-hPa and 500-hPa temperature (T200–T500), with a minimum threshold of $\geq$ 0.6 K, and a separation distance $\leq 6.5^\circ$ with offset $\leq 1.0^\circ$. Candidate centers are merged within 6.0° and filtered based on sustained 10-meter wind speeds reaching tropical storm strength ($\geq$ 34 knots), surface topography $\leq$ 150 m, latitude $\leq 50^\circ$, and a minimum lifetime of 24 hours. A detailed description of the EAMv2 simulations is provided in Table 1.

https://doi.org/10.5194/egusphere-2025-4277
Preprint. Discussion started: 21 October 2025

components: potential intensity (V_{pot}), mid-tropospheric (600-hPa) relative humidity (RH), and vertical wind shear between 850 and 200 hPa (V_{shear}). The absolute vorticity term (η) is excluded from the figure due to its relatively minor contribution compared to the other components. These diagnostics follow the formulation of Emanuel (2004) (see Appendix A), which provides a quantitative framework for linking environmental conditions to TC genesis. Higher GPI values correspond to more favorable genesis conditions, typically associated with stronger V_{pot}, higher RH, and weaker V_{shear}. The free-running EAMv2 simulation (CLIM; panel a1) exhibits substantial GPI biases, driven by a combination of thermodynamic (panels a2–a3) and dynamical (panel a4) deficiencies. These biases persist in simulations that only reduce dynamical errors (panels b1–b4) or apply partial constraints on thermodynamic variables (panels c1–c4). In contrast, the simulation that applies constraints to both dynamical (U, V) and thermodynamical (T, Q) fields (panels d1–d4) more accurately reproduces the observed GPI climatology. These results highlight the importance of simultaneously constraining both types of fields to improve the model representation of large-scale environmental conditions associated with storms like TCs.

In addition, the results in Fig. 8 highlight that the substantial storm track density biases over the Atlantic and Eastern Pacific (Fig. 7) are partly driven by an overestimation of vertical wind shear in the lower latitudes of these basins in the CLIM simulation. This interpretation is supported by the NDG-UV experiment, where nudging of horizontal winds reduces the shear biases (Fig. 8b4) and leads to a corresponding increase in TC genesis events (Fig. C4c). However, additional nudging of temperature and humidity does not result in further improvement in TC genesis, suggesting that the remaining deficiencies primarily stem from the coarse resolution of EAMv2, which limits its ability to resolve the dynamics essential for tropical cyclone formation. Nevertheless, constraining both dynamical and thermodynamical fields is essential for improving the model's simulation of the seasonal and annual cycle of the Genesis Potential Index (GPI; Fig.9). Among all experiments, the NDG-UVTQ_SRF1 simulation (red lines,Fig.9), which includes additional constraints on near-surface humidity, most effectively reproduces the observed variability and seasonal peaks of GPI across all tropical cyclone basins, with the closest agreement to ERA5 (black lines, Fig.9). This indicates that accurately constraining both dynamical and thermodynamical conditions in numerical models was essential for representing the large-scale environment relevant to tropical cyclones. Given the strong statistical relationship between GPI and TC genesis density (r in Fig. 9), these results demonstrate the importance of realistically simulating the large-scale temperature and humidity fields that support TC development. In particular, the humidity nudging strategy proposed in this study provides a practical approach to improving thermodynamic field representation, thereby enabling more reliable TC downscaling from low-resolution GCMs such as EAMv2.

Further analysis of two additional high-impact weather phenomena, namely extratropical cyclones (ETCs) and atmospheric rivers (ARs), reveals that the benefits of the proposed nudging strategy extend beyond tropical cyclones. Figure 10 presents the seasonal cycle of ETC occurrence frequency and the subset of intense ETCs (defined as those with central pressure below 990 hPa), derived from TempestExtremes tracking of 6-hourly EAMv2 output from the experiments listed in Table 1. The results are averaged over the Northern (panels a–b) and Southern (panels c–d) Hemispheres, respectively, as defined according to the climatological distribution of extratropical cyclones (see Fig. C5). Compared to the free-running (CLIM) and wind-only nudged (NDG-UV) simulations, the NDG-UVT and NDG-UVTQ configurations, which include additional nudging of temperature and humidity, show improved agreement with ERA5 in capturing the seasonal variability of ETC frequency in

https://doi.org/10.5194/egusphere-2025-4277
Preprint. Discussion started: 21 October 2025

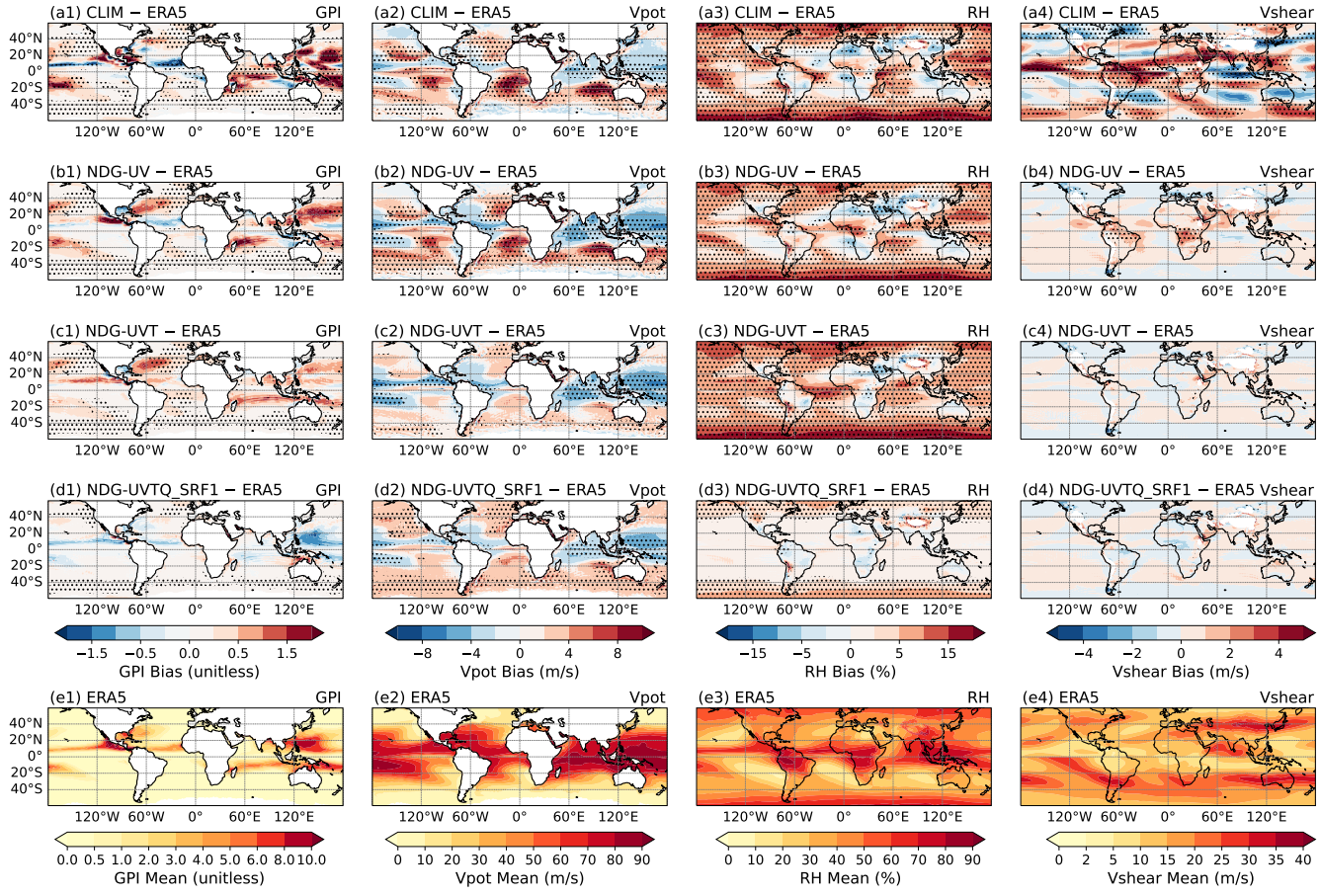

Figure 8. Spatial distribution of the Genesis Potential Index (GPI) and its components in free-running and nudged EAMv2 simulations compared to ERA5 reanalysis over the period 2008–2017. The first four rows show seasonal-mean biases (experiment minus ERA5) for GPI and its key components—potential intensity (V_{pot}), mid-tropospheric relative humidity (RH at 600 hPa), and vertical wind shear (200–850 hPa)—across three EAMv2 configurations. Stippling marks regions where differences from ERA5 are statistically significant at the 95% confidence level based on a two-sample t-test. The bottom row displays corresponding seasonal-mean climatologies from ERA5 for each variable. Colored contours represent variable values, while transparent filled circles denote observed tropical cyclone (TC) genesis locations from the IBTrACS dataset during the same period. GPI and component averages are computed using seasonally adjusted months—June to November for the Northern Hemisphere and November to May for the Southern Hemisphere—to reflect TC activity timing. Panel labels are organized as (a1)–(d3) for biases and (e1)–(e4) for ERA5 mean fields. A detailed description of the EAMv2 simulations is provided in Table 1.

https://doi.org/10.5194/egusphere-2025-4277
Preprint. Discussion started: 21 October 2025

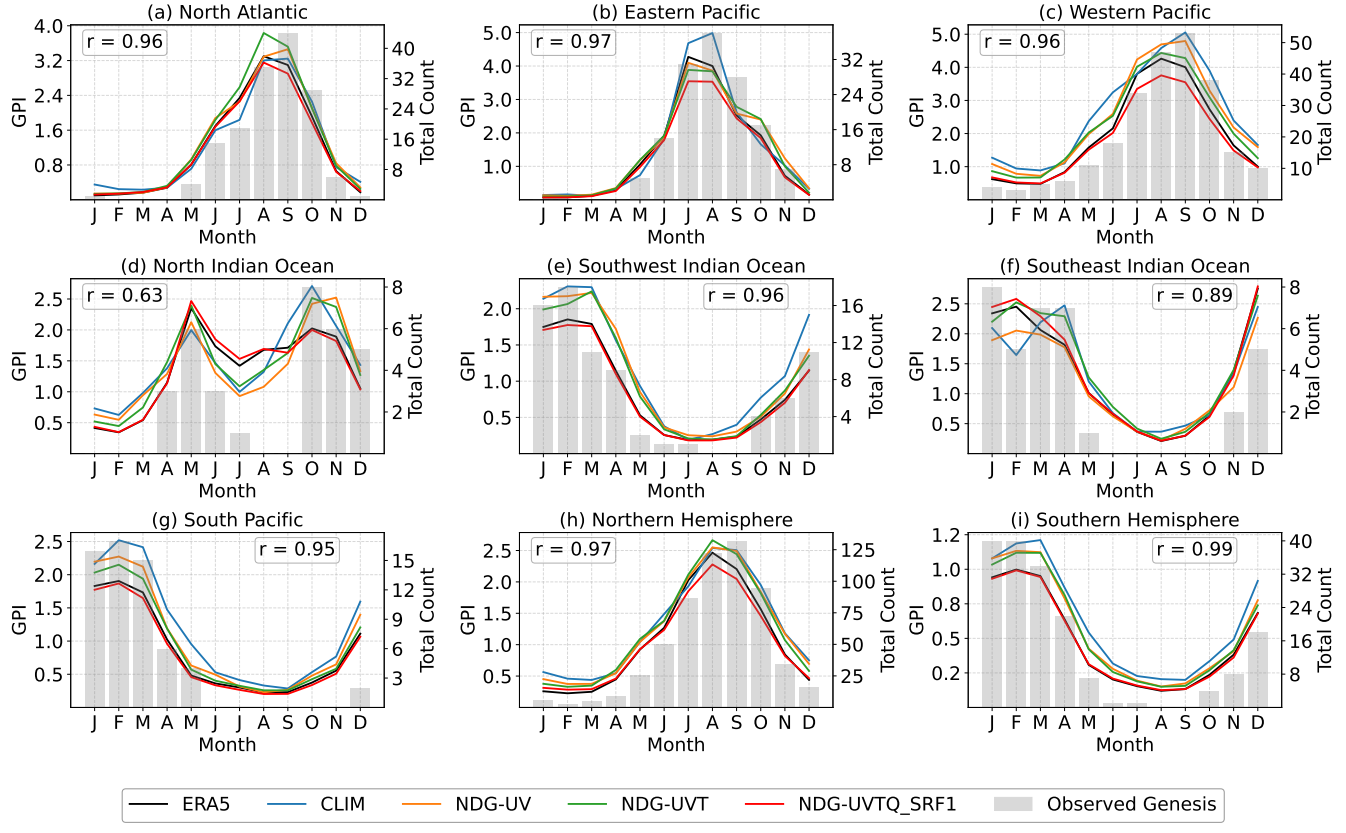

Figure 9. Seasonal cycle of the Genesis Potential Index (GPI), derived using Eq.(A1), and observed tropical cyclone (TC) genesis counts across major ocean basins during the period 2008–2017. Colored lines show GPI values computed from ERA5 reanalysis (black) and various EAMv2 free-running and nudged simulations (colored), each averaged over TC basin regions defined according to WMO standards (WMO, 2017). Gray bars indicate observed monthly TC genesis counts from the IBTrACS dataset (Knapp et al., 2010), aggregated within each basin. Twin y-axes are used to depict GPI (left axis) and TC genesis frequency (right axis). The correlation coefficient (r) between the annual cycle of GPI from ERA5 and TC genesis counts from IBTrACS is also shown for each basin as a reference. The basins are defined as follows: North Atlantic (0–45°N, 100–10°W), Eastern Pacific (0–35°N, 140–100°W), Western Pacific (0–45°N, 100–180°E), North Indian Ocean (0–30°N, 40–100°E), Southwest Indian Ocean (40–0°S, 30–100°E), Southeast Indian Ocean (40–0°S, 100–135°E), and South Pacific (40–0°S, 135°E–100°W). Two additional hemispheric averages are also included: Northern Hemisphere (0–60°N, global) and Southern Hemisphere (60–0°S, global). A detailed description of the EAMv2 simulations is provided in Table1.

https://doi.org/10.5194/egusphere-2025-4277
Preprint. Discussion started: 21 October 2025

both hemispheres. These improvements are especially notable for intense ETCs, where NDG-UVT and NDG-UVTQ reduce the overestimation of storm frequency during the boreal summer (JJA) and correct the underestimation during the boreal winter (DJF) in the Northern Hemisphere, while also partially mitigating the underrepresentation of intense ETCs in the Southern Hemisphere. The results highlight the role of large-scale thermodynamic fields in shaping ETC climatology and support the utility of full-field nudging for improving storm-track variability and extremes in low-resolution models.

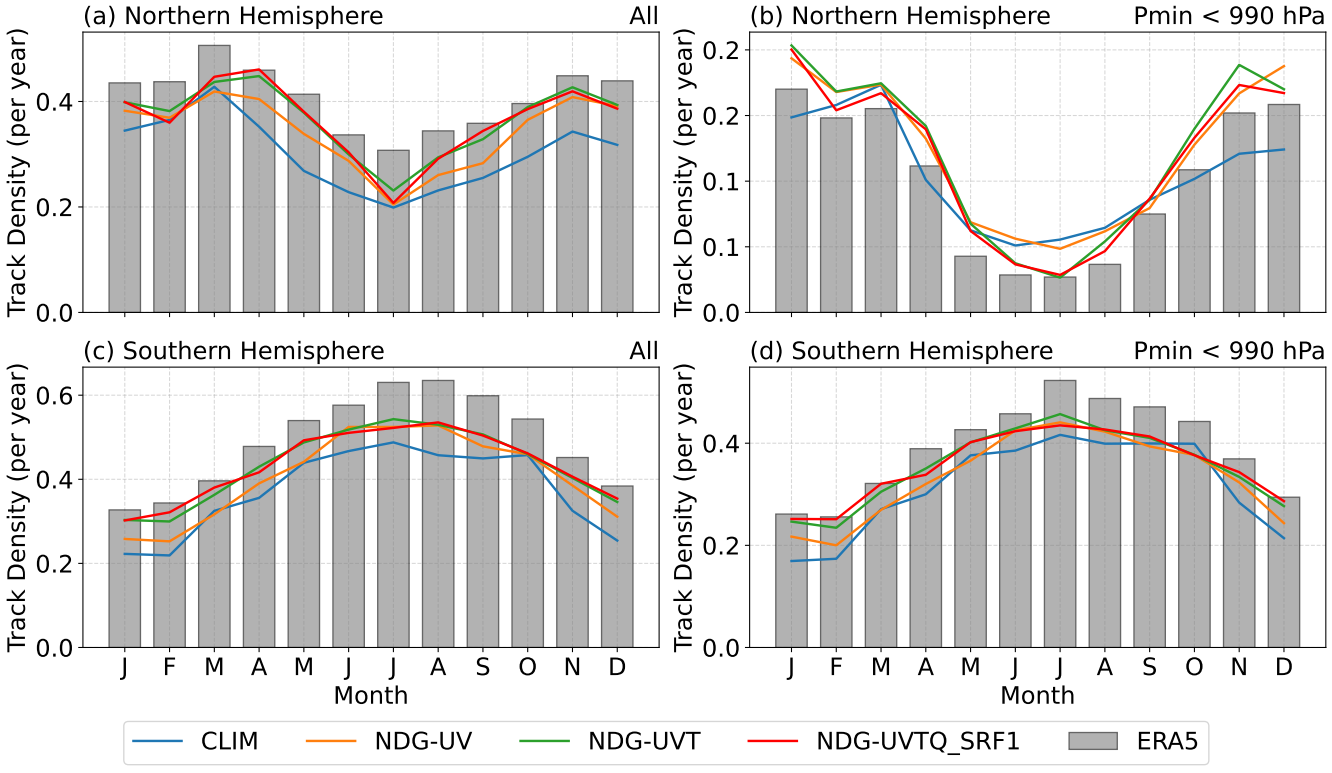

Figure 10. Seasonal cycle of extratropical cyclone (ETC) track density averaged over the Northern Hemisphere (20°–90°N) and Southern Hemisphere (20°–90°S), based on ERA5 reanalysis and EAMv2 simulations during 2008–2017. Bars indicate the monthly climatology from ERA5, and colored lines represent individual model simulations. Two track definitions based on minimum sea-level pressure (P_{min}) thresholds are shown: (left) all identified ETC-like vortices, and (right) intense ETCs with P_{min} below 990 hPa. Cyclone detection is performed using the TempestExtremes algorithm (Ullrich et al., 2021), applied to 6-hourly sea-level pressure (PSL) fields. Candidate cyclone centers are first identified as local PSL minima enclosed by closed contours, defined as regions where PSL increases by at least 200 Pa within a 5.5° great-circle radius, following the `--closedcontourcmd` criterion in TempestExtremes. Tracks are constructed by linking features that travel no more than 9.0° per 6-hour interval, with a minimum lifetime of 60 hours and a maximum temporal gap of 18 hours. Tropical cyclone-like vortices identified in Figure 7 are excluded. Track density is computed by counting cyclone centers within 5° × 5° grid cells and averaging over each hemisphere. Monthly values represent the total number of ETCs per month. Details of the EAMv2 simulations are provided in Table 1.

https://doi.org/10.5194/egusphere-2025-4277
Preprint. Discussion started: 21 October 2025

In contrast to tropical cyclones (TCs) and extratropical cyclones (ETCs), atmospheric rivers (ARs) are characterized by large-scale water vapor transport governed by both wind and humidity fields—processes that EAMv2 is capable of explicitly resolving. A realistic representation of AR occurrence and its variability, therefore, requires accurate simulation of both dynamical and thermodynamic components. As shown in Fig. 11, the discrepancies in AR occurrences between the CLIM simulation and ERA5 across all major AR-active basins are systematically reduced as EAMv2 is incrementally constrained toward ERA5's wind, temperature, and humidity fields. Consistently, a systematic reduction in the biases of the long-term mean spatial distribution of AR frequencies is also observed across the nudged simulations (Fig. C6). Among the different nudging strategies, constraining humidity is shown to be particularly important for achieving realistic AR occurrence frequency and seasonal variability in GCMs like EAMv2, especially over the Northeast Pacific and North Atlantic regions.

Overall, the results in this section indicate that the nudged EAMv2 simulations, particularly those incorporating additional humidity nudging as proposed in this study, substantially improve the model's representation of large-scale environmental conditions associated with high-impact weather systems. By conducting a series of hindcast simulations in which wind, temperature, and humidity fields are incrementally constrained toward observations, we are able to isolate and assess the contributions of dynamic and thermodynamic biases to the simulated large-scale environment relevant for tropical cyclone development. Comparisons between simulations with and without humidity nudging further underscore the critical role of large-scale moisture fields in capturing the seasonal variability of high-impact weather phenomena—including tropical cyclones, extratropical cyclones, and atmospheric rivers—in low-resolution GCMs. These findings demonstrate that the proposed nudging strategy offers an observationally constrained framework that minimizes disruption to the model's physical balances, supporting the study of extreme atmospheric events and aligning with the objectives emphasized in Wehrli et al. (2022).

6 Conclusions

This study presents an improved nudging strategy for the E3SM Atmosphere Model version 2 (EAMv2), extending the commonly used wind-field nudging (U, V) to also include temperature (T) and humidity (Q) constraints. The revised formulation modulates nudging tendencies in the upper and lower atmosphere based on pressure and boundary-layer height, thereby reducing artificial distortions near the model top and surface. We evaluate this approach through a suite of atmospheric hindcast experiments with EAMv2, forced by observed sea surface temperature and sea ice concentrations. In these experiments, where U, V, T, and Q were selectively nudged toward ERA5 reanalysis, the strategy enables effective thermodynamic nudging while better preserving internal physical balances and limiting spurious distortions in key simulated fields, including precipitation and radiative fluxes.

Our results show that simultaneous nudging of wind, temperature, and humidity significantly improves the fidelity of the simulated large-scale thermodynamic state. Compared to wind-only or wind-and-temperature nudging, the inclusion of humidity constraints reduces biases in total precipitable water, outgoing longwave radiation, and precipitation. These improvements are particularly pronounced in tropical regions, where realistic moisture fields are essential for capturing convective processes and precipitation variability. Previous studies have reported that nudging temperature and humidity can degrade the hydrolog-

https://doi.org/10.5194/egusphere-2025-4277
Preprint. Discussion started: 21 October 2025

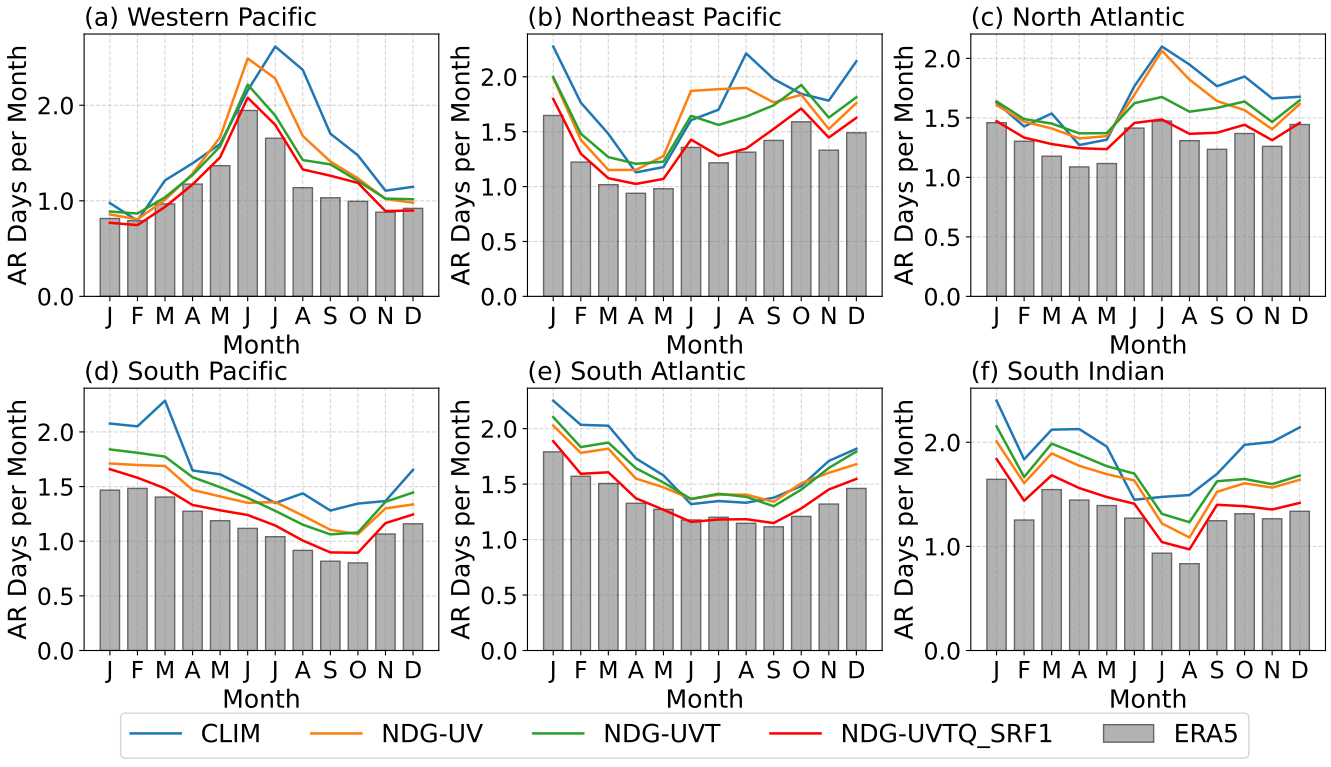

Figure 11. Monthly climatology of atmospheric river (AR) occurrence frequency from ERA5 and EAMv2 simulations during 2008–2017, averaged over six ocean basins: Western Pacific, Northeast Pacific, North Atlantic, South Pacific, South Atlantic, and South Indian Ocean. Bars represent ERA5 reanalysis, and solid lines indicate model simulations. ARs are detected using the TempestExtremes algorithm (Ullrich et al., 2021), applied to 6-hourly vertically integrated moisture fluxes (TUQ and TVQ). Detection is based on the Laplacian of integrated vapor transport (IVT) magnitude, which highlights filamentary structures by identifying local maxima. Features are retained if the Laplacian is ≤ -40000, the area exceeds 400,000km^2, and the feature occurs equatorward of 75° latitude ($|\text{lat}| \geq 15°$). Basin definitions follow rectangular latitude–longitude domains adapted from Tier1 regions of the ARTMIP project (Rutz et al., 2019), and are defined as follows: Western Pacific (0–45°N, 120–180°E), Northeast Pacific (20–60°N, 180–240°E), North Atlantic (20–60°N, 270–330°E), South Pacific (60–20°S, 160–240°E), South Atlantic (60–20°S, 300–360°E), and South Indian Ocean (50–20°S, 40–120°E). A detailed description of the EAMv2 simulations is provided in Table 1.

https://doi.org/10.5194/egusphere-2025-4277
Preprint. Discussion started: 21 October 2025

ical cycle in EAM simulations (Sun et al., 2019), underscoring the challenge of applying thermodynamic constraints without disrupting dynamical and thermodynamical balances. The revised nudging strategy introduced here addresses this issue by objectively limiting the influence of nudging to levels above the time-varying top of the planetary boundary layer (PBL), allowing near-surface processes to respond freely to local conditions. This approach enables effective large-scale constraints while supporting a more realistic representation of the hydrological cycle.

Furthermore, we find that extending nudging to include surface-layer variables enhances land–atmosphere coupling and improves agreement with ERA5 reanalysis for surface-related processes. This extension reduces the spurious impacts of humidity nudging on longwave radiative fluxes and precipitation, highlighting the value of surface constraints in complementing upper-atmosphere nudging while minimizing disruption to the model's intrinsic physical relationships. Meanwhile, compared to NDG-UVTQ, the additional surface-layer nudging in NDG-UVTQ_SRF1 provides only limited benefits for large-scale dynamical features such as moisture convergence. This distinction suggests that the primary improvements in surface diagnostics result from a more accurate representation of the large-scale thermodynamic state, rather than from direct corrections to surface-layer dynamics.

Beyond the evaluation of long-term mean model biases, the improved nudging strategy enhances EAMv2's ability to represent large-scale environmental conditions associated with high-impact weather systems. By conducting a series of nudged simulations that progressively constrain subsets of model state variables (U, V, T, and Q), we can assess the relative contributions of dynamical and thermodynamical processes to model biases in key diagnostic fields, such as the Genesis Potential Index (GPI), which is closely linked to tropical cyclone (TC) development. The results show that both dynamical (e.g., vertical wind shear) and thermodynamical (e.g., potential intensity, mid-tropospheric humidity) factors contribute to GPI biases. In particular, realistic thermodynamic conditions are found to be essential for capturing the seasonal evolution of GPI, underscoring their importance in representing the variability of large-scale environmental conditions associated with TCs. These findings further extend to the simulation of other high-impact phenomena, including the seasonal variability of atmospheric rivers and extratropical cyclone activity. Collectively, these results demonstrate that effective temperature and humidity nudging offers a valuable approach for studying extreme weather events in global models, particularly those with limited horizontal resolution where such events must be inferred from large-scale storm environments.

Watt-Meyer et al. (2021) reported that nudging specific humidity in hindcast simulations induced a drying effect in the atmospheric column, which in turn suppressed surface precipitation. When these simulations were subsequently used to train a machine learning (ML) bias-correction method, the ML-predicted humidity corrections reproduced the same drying tendency, ultimately degrading precipitation performance. These results illustrate the risk that humidity nudging may inadvertently alter the model's mean state and physical balances, thereby reducing the reliability of ML models trained on such data. In contrast, as shown in Section 4, the humidity-nudging formulation introduced here avoids such impacts on the hydrological cycle and instead improves hindcast skill for precipitation. By better preserving thermodynamic and hydrological consistency, this approach provides nudged hindcast data that offer a more robust foundation for training ML-based bias-correction methods, including those proposed by Watt-Meyer et al. (2021).

https://doi.org/10.5194/egusphere-2025-4277
Preprint. Discussion started: 21 October 2025

Overall, the proposed approach enables more accurate and consistent hindcasts, supporting applications ranging from model evaluation to the generation of training datasets for machine learning. Future efforts should explore the retuning of microphysical parameterizations for use in nudged configurations and assess the generality of these findings across other model resolutions and Earth system components.

https://doi.org/10.5194/egusphere-2025-4277
Preprint. Discussion started: 21 October 2025

Appendix A: Tropical Cyclone Genesis Potential Index

The Genesis Potential Index (GPI) proposed by Emanuel (2004) provides a quantitative measure of the favorable environmental conditions for tropical cyclone genesis. It combines contributions from absolute vorticity, mid-level humidity, potential intensity, and vertical wind shear as follows:

$$\mathrm{GPI} = \left(10^5 \cdot |\eta|\right)^{3/2} \cdot \left(\frac{\mathrm{RH}}{50}\right)^3 \cdot \left(\frac{V_{\mathrm{pot}}}{70}\right)^3 \cdot (1 + 0.1 \cdot V_{\mathrm{shear}})^{-2} \tag{A1}$$

Where η is the absolute vorticity at 850 hPa (s^{-1}), RH is the relative humidity at 600 hPa (in %), V_{pot} is the potential intensity ($\mathrm{m\,s}^{-1}$), and V_{shear} is the magnitude of the vertical wind shear between 850 hPa and 200 hPa ($\mathrm{m\,s}^{-1}$). The constants are chosen to nondimensionalize the variables and appropriately scale the index.

https://doi.org/10.5194/egusphere-2025-4277
Preprint. Discussion started: 21 October 2025

Appendix B: Additional Tables

Table B1. List of physical quantities used for diagnostics in Fig. 4 and Fig. C1. The fifth column lists the reference datasets used to derive the error metrics, primarily sourced from ERA5 reanalysis (Hersbach et al., 2020), GPCP (Version 2.3; Adler et al., 2003), and CERES_EBAF (Version 4.1; Kato et al., 2018).

Variable	Description	Level	Unit	Reference
Atmospheric State Variables				
U200, U500, U850	Zonal wind	200–850 hPa	m s^{-1}	ERA5
V200, V500, V850	Meridional wind	200–850 hPa	m s^{-1}	ERA5
T200, T500, T850	Temperature	200–850 hPa	K	ERA5
Q200, Q500, Q850	Specific humidity	200–850 hPa	g kg^{-1}	ERA5
W200, W500, W850	Vertical velocity (pressure)	200–850 hPa	Pa s^{-1}	ERA5
Z200, Z500, Z850	Geopotential height	200–850 hPa	hectometer	ERA5
Surface Variables and Energy Fluxes				
SLP	Sea level pressure	Surface	hPa	ERA5
T2M	Surface air tempature	Surface	K	ERA5
TS	Surface skin tempature	Surface	K	ERA5
SHFLX, LHFLX	Sensible / Latent heat flux	Surface	W m^{-2}	ERA5
Precipitation and Moisture				
PRECT	Total precipitation rate	Surface	mm day^{-1}	GPCP
PRECST	Total snow rate	Surface	mm day^{-1}	ERA5
TMQ	Total precipitable water	Column	kg m^{-2}	ERA5
Radiative Fluxes (TOA/Surface)				
FLUT, FLUTC	Upwelling longwave (TOA)	TOA	W m^{-2}	CERES_EBAF
FLNT, FLNTC	Net longwave flux (TOA)	TOA	W m^{-2}	CERES_EBAF
FSNT, FSNTC	Net shortwave flux (TOA)	TOA	W m^{-2}	CERES_EBAF
SWCF, LWCF	Shortwave / Longwave cloud forcing	TOA	W m^{-2}	CERES_EBAF
FLDS, FLDSC	Downward longwave flux	Surface	W m^{-2}	CERES_EBAF
FLNS, FLNSC	Net surface longwave flux	Surface	W m^{-2}	CERES_EBAF
FSNS, FSNSC	Net surface shortwave flux	Surface	W m^{-2}	CERES_EBAF
Cloud Properties				
CLDTOT	Total cloud fraction	Column	%	CERES_EBAF
LWP	Total cloud liquid water path	Column	kg m^{-2}	ERA5
IWP	Total cloud ice water path	Column	kg m^{-2}	ERA5

https://doi.org/10.5194/egusphere-2025-4277
Preprint. Discussion started: 21 October 2025

Appendix C: Additional figures

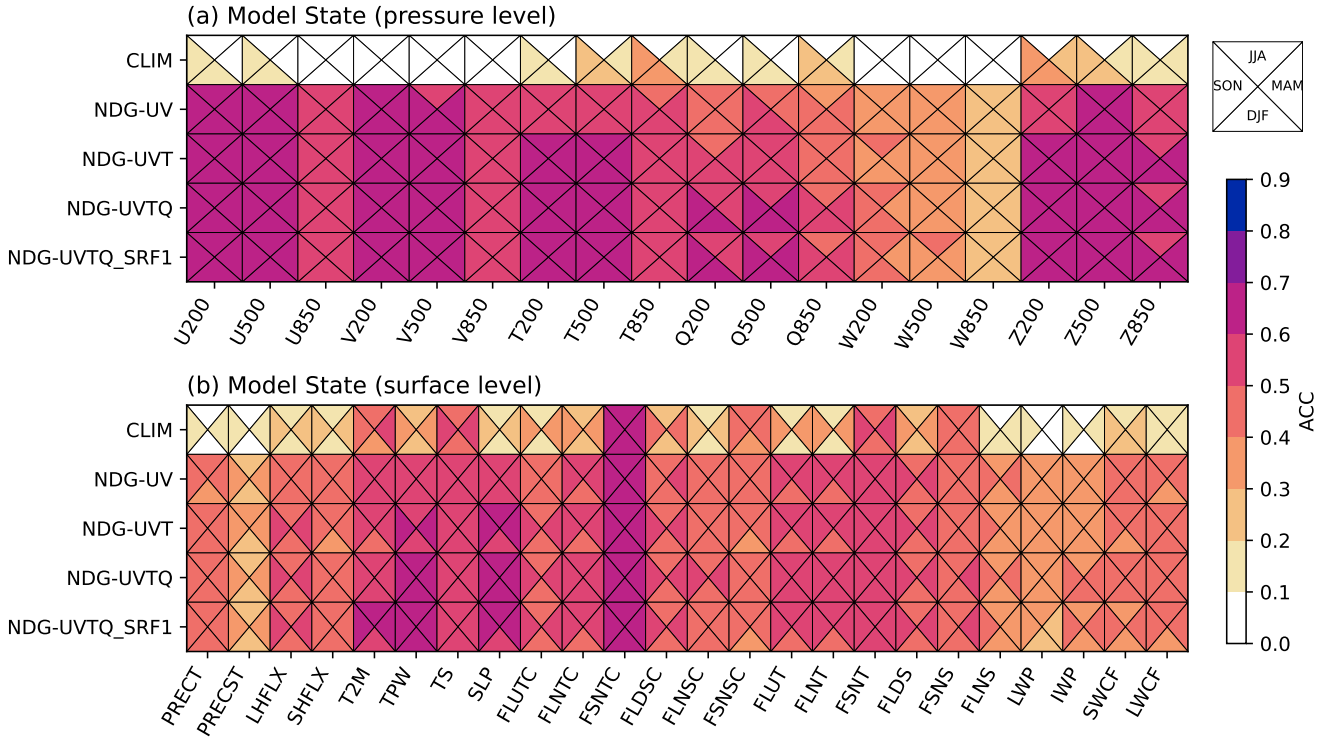

Figure C1. Same as Figure 4, but for anomaly correlation coefficients (ACC) between observations and EAMv2 simulations listed in Table 1. Seasonal anomalies were computed by subtracting the time-mean climatology at each grid point from both model and observational data. Pearson correlation coefficients were then calculated across time at each location to obtain a gridded ACC field. These values were weighted by the cosine of latitude and averaged globally to produce a single ACC per variable and experiment, shown in the figure. Definitions of the physical quantities and their corresponding reference datasets are provided in Table B1.

https://doi.org/10.5194/egusphere-2025-4277
Preprint. Discussion started: 21 October 2025

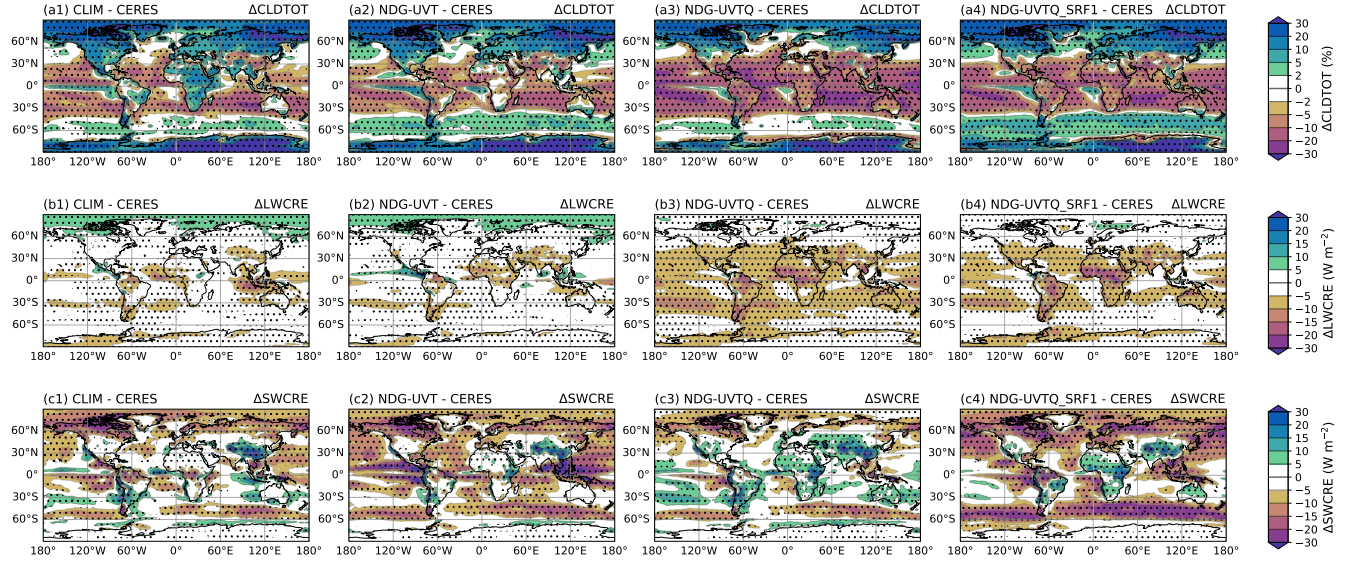

Figure C2. Same as Figure C3, but for horizontal distribution of annual mean model biases in total cloud fraction (CLDTOT, units: %; panels a1–a3), shortwave cloud radiative effect (SWCRE, units: W m^{-2}; panels b1–b3), and longwave cloud radiative effect (LWCRE, units: W m^{-2}; panels c1–c3), averaged over the period 2008–2017. Details of the simulation setups are provided in Table 1.

https://doi.org/10.5194/egusphere-2025-4277
Preprint. Discussion started: 21 October 2025

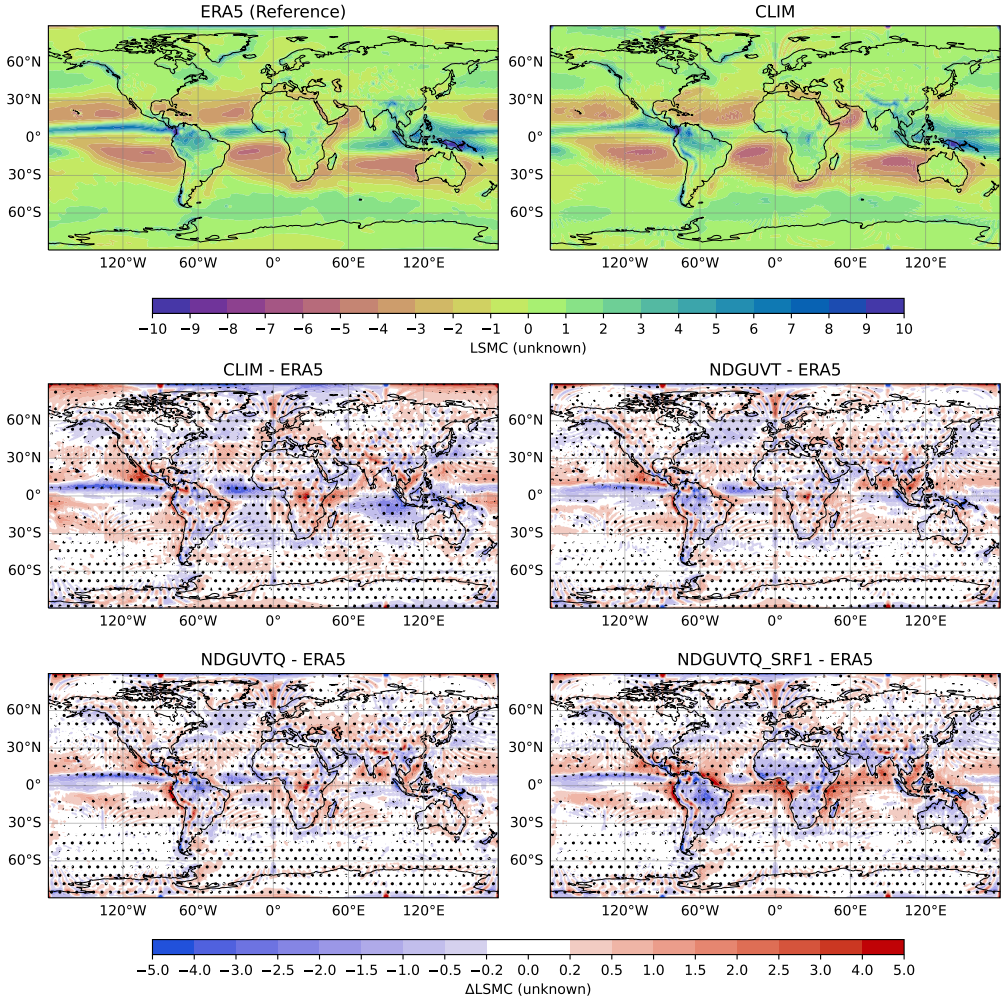

Figure C3. Spatial patterns of annual mean large-scale moisture convergence (LSMC) and differences between EAMv2 simulations and observations, averaged over the 10 years from 2008 to 2017. Panels **(a–b)** show Annual mean LSMC from ERA5 (reference) and CLIM simulation using EAMv2, respectively. Panels **(c–f)** show differences in annual mean LSMC between the reference and CLIM or nudged model experiments, where positive values indicate greater moisture convergence in the model relative to ERA5. LSMC was derived from vertically integrated zonal and meridional moisture fluxes at 6-hourly frequency. After derivation, a 1° Gaussian filter was applied to the spatial fields to reduce noise. The 6-hourly LSMC was then averaged over each year to obtain a 10-year climatological mean. Stippling indicates grid points where model–reference differences are statistically significant at the 95% confidence level based on a two-sided Student *t*-test. Details of the EAMv2 simulations are summarized in Table 1.

https://doi.org/10.5194/egusphere-2025-4277
Preprint. Discussion started: 21 October 2025

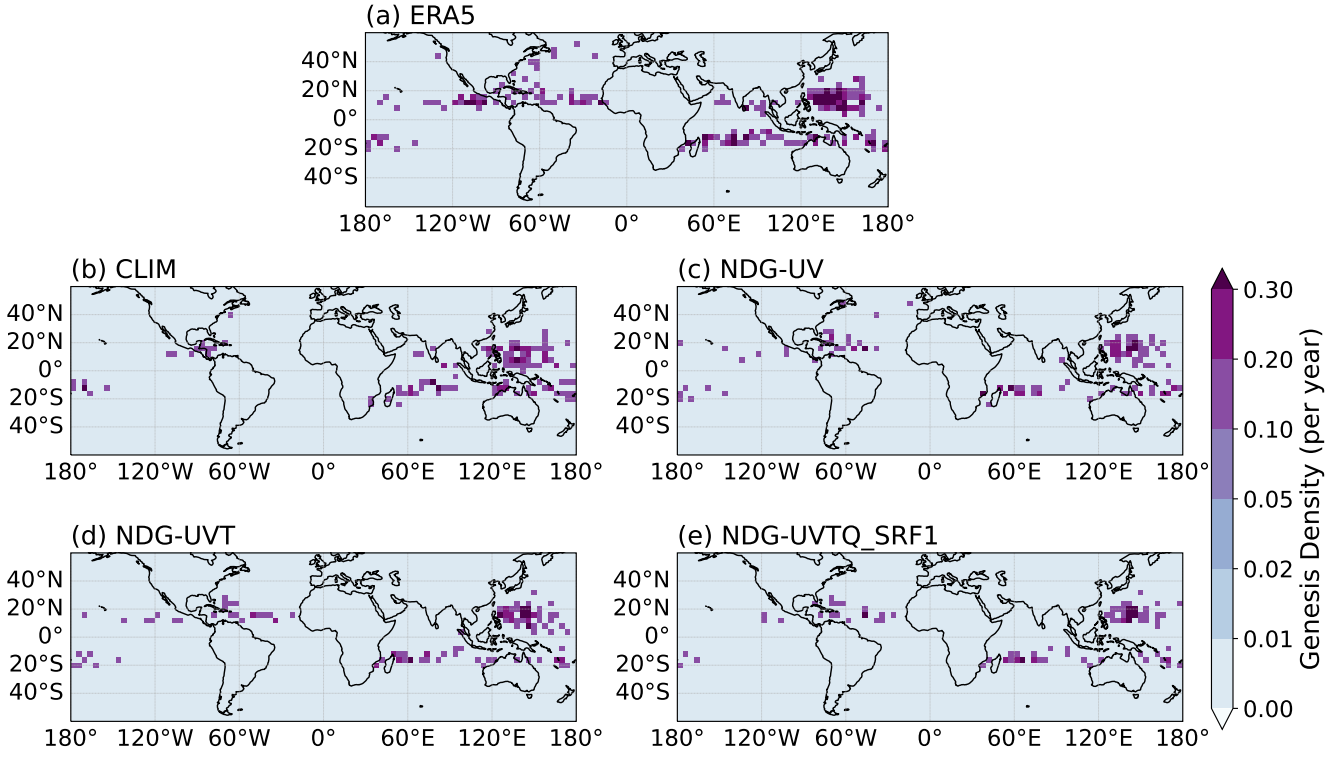

Figure C4. Same as Figure 7, but for tropical cyclone genesis densities tracked by TempestExtremes using ERA5 and E3SM simulations over the period 2008–2017. Cyclone genesis is defined as the first point along each storm track that meets the detection criteria. A detailed description of the EAMv2 simulations is provided in Table 1.

https://doi.org/10.5194/egusphere-2025-4277
Preprint. Discussion started: 21 October 2025

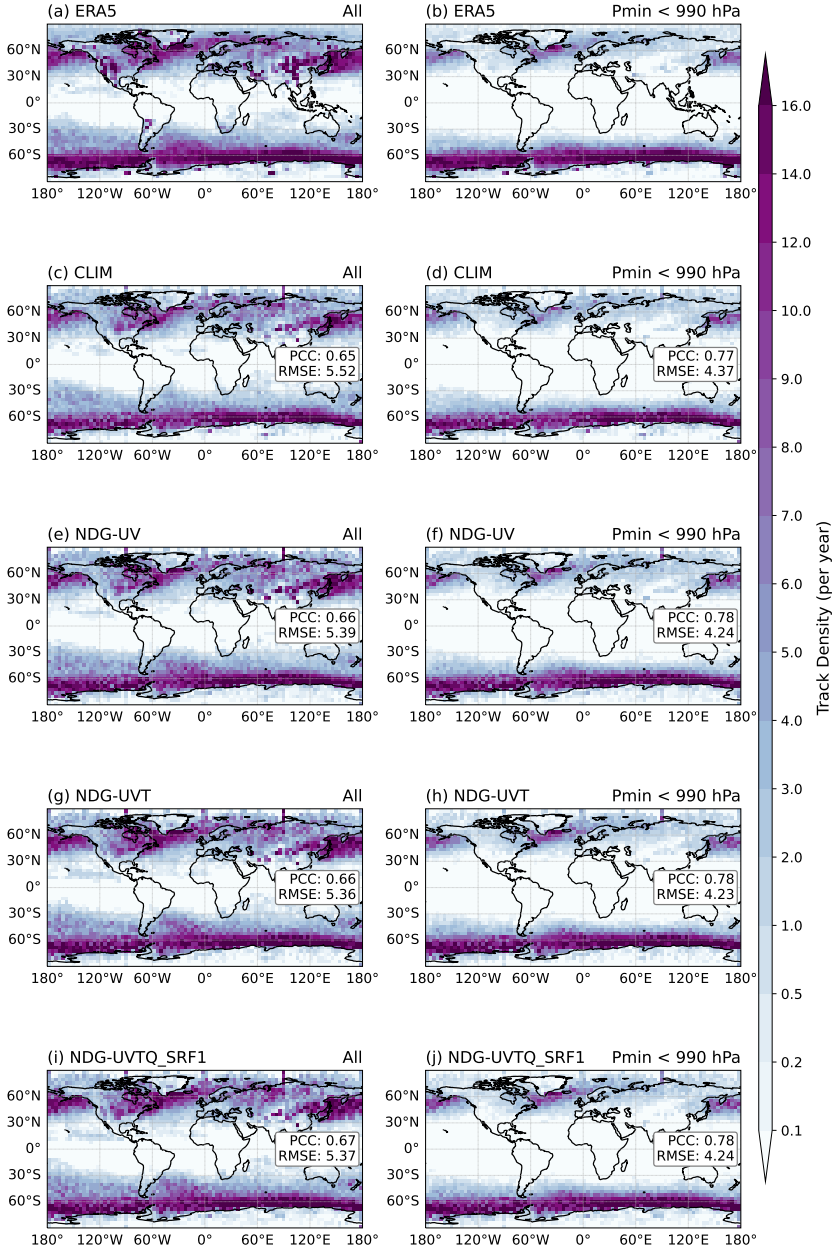

Figure C5. Climatological spatial distribution of extratropical cyclone (ETC) track density from ERA5 reanalysis and EAMv2 model simulations during 2008–2017. Each panel shows the mean annual ETC track density (number of cyclones per $4^\circ \times 4^\circ$ grid box per year), with ERA5 shown in the top row and model biases (simulation minus ERA5) in subsequent rows. Results are based on TempestExtremes tracking using two criteria: (left) all identified ETC tracks and (right) tracks with minimum sea-level pressure (P_{min}) below 990 hPa. All tropic-cyclone-like vortices, as shown in Figure 7, were excluded from ETCs. Colored contours represent cyclone density, and pattern correlation (PCC) and root-mean-square error (RMSE) statistics relative to ERA5 are annotated in each model panel. A detailed description of the EAMv2 simulations is provided in Table 1.

https://doi.org/10.5194/egusphere-2025-4277
Preprint. Discussion started: 21 October 2025

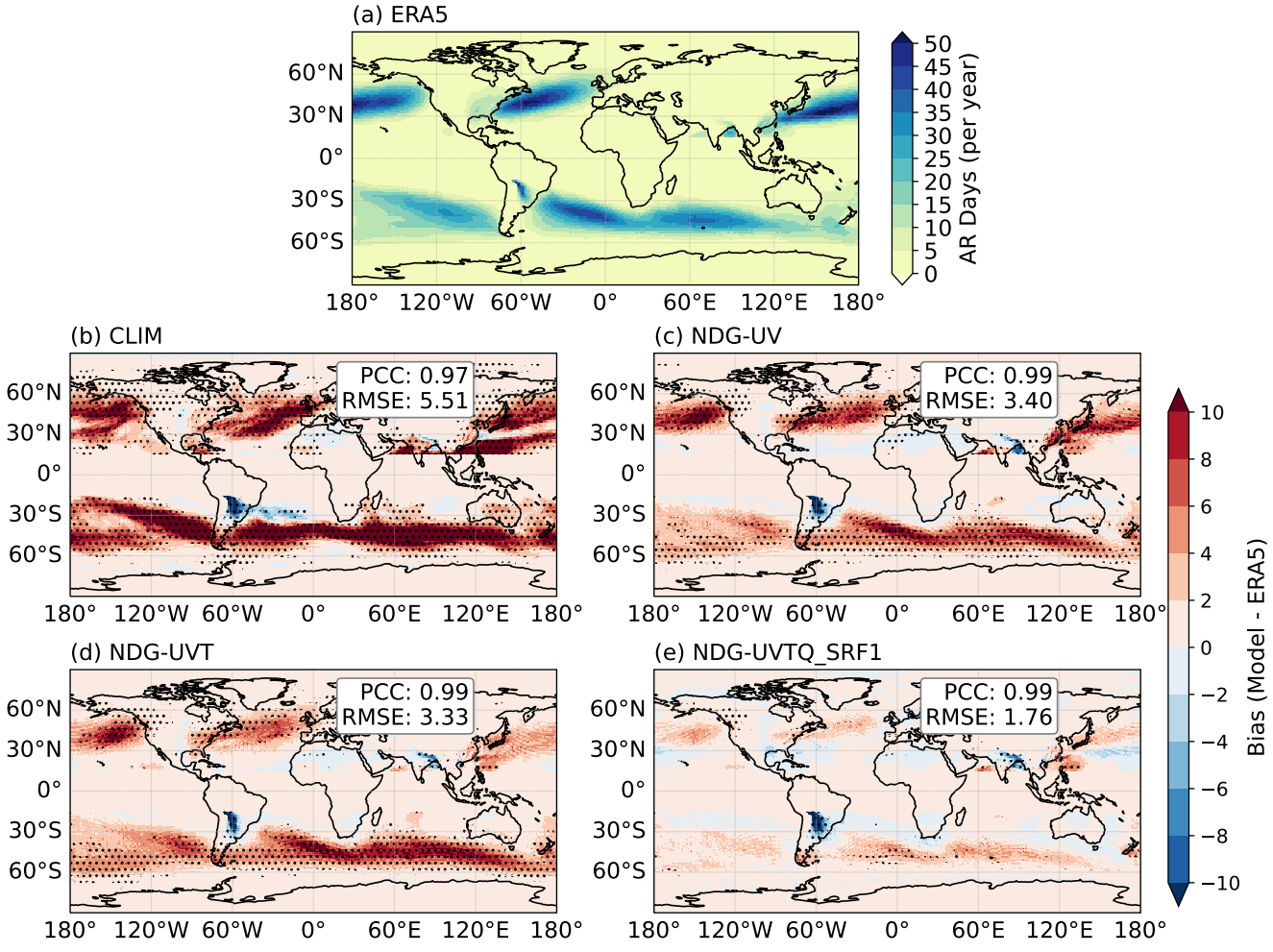

Figure C6. Climatological annual mean atmospheric river (AR) occurrence frequency from ERA5 and EAMv2 simulations during 2008–2017. The top panel shows the ERA5 reference in AR days per year, and the lower panels show model biases (model minus ERA5). Stippling indicates regions where the differences are statistically significant at the 95% confidence level based on a two-sample Student's t-test. Colored contours represent cyclone density, and pattern correlation (PCC) and root-mean-square error (RMSE) values relative to ERA5 are annotated in each model panel. ARs were identified using the same tracking algorithm described in Figure 10. A detailed description of the EAMv2 simulations is provided in Table 1.

https://doi.org/10.5194/egusphere-2025-4277
Preprint. Discussion started: 21 October 2025

Code availability. The source code for EAMv2 (E3SM Project, U.S. Department of Energy, 2021) was from the Energy Exascale Earth System Model project, sponsored by the U.S. Department of Energy, Office of Science, Office of Biological and Environmental Research. The revised model code with all changes discussed in this study can be found on Zenodo at https://doi.org/10.5281/zenodo.5532605 (Zhang, 2025a). The TempestExtremes package used for feature tracking of high-impact weather events was extracted from the Github at https://github.com/ClimateGlobalChange/tempestextremes (Ullrich, 2022), and the user guide for this package can be found at https://climate.ucdavis.edu/tempestextremes.php (Ullrich et al., 2021).

Data availability. The data used to produce the figures in this paper are archived on Zenodo at https://doi.org/10.5281/zenodo.17015705 (Zhang, 2025b). The ERA5 reanalysis data used for nudging and evaluation in this study are available from the Copernicus Climate Change Service (C3S) Climate Data Store at https://doi.org/10.24381/cds.bd0915c6 (Hersbach et al., 2018a) and https://doi.org/10.24381/cds.adbb2d47 (Hersbach et al., 2018b). Satellite datasets used for analysis in this study were obtained from the following sources:

- Tropical Rainfall Measuring Mission (TRMM) 3B42 Version 7 Precipitation Product (Huffman and Bolvin, 2015);
- Global Precipitation Climatology Project (GPCP) Version 3.2 Product (Adler et al., 2003);
- Clouds and the Earth's Radiant Energy System (CERES) Energy Balanced and Filled (EBAF) Edition 4.0 Product (Kato et al., 2018);

Author contributions. S. Z., R. L., and B. H. led the conceptualization of the study. S. Z. designed the study, implemented the temperature and humidity nudging strategy in EAMv2, conducted the hindcast experiments, performed the analysis, and wrote the initial manuscript draft. R. L. supervised the project, contributed to the experimental design, and provided substantial input to manuscript revisions. B. H. assisted with model configuration and post-processing of simulation outputs. B. H. and K. Z. contributed substantially to manuscript revisions. A. B., G. K., and K. S. contributed to the refinement of the revised nudging methodology and provided feedback on the manuscript. All authors discussed the results and contributed to the final version of the manuscript.

Competing interests. The authors declare no competing interests

Acknowledgements. This research was supported by the Scalable, Efficient and Accelerated Causal Reasoning Operators, Graphs and Spikes for Earth and Embedded Systems (SEA-CROGS) project, funded by the Office of Science, U.S. Department of Energy, Advanced Scientific Computing Research (ASCR) program. Computing resources for the simulations were provided by the National Energy Research Scientific Computing Center (NERSC), a DOE Office of Science User Facility at Lawrence Berkeley National Laboratory, operated under Contract No. DE-AC02-05CH11231. PNNL is operated by Battelle Memorial Institute for the DOE under Contract No. DE-AC05-76RL01830. The authors acknowledge the use of ChatGPT (OpenAI) to refine the wording of the manuscript.

https://doi.org/10.5194/egusphere-2025-4277
Preprint. Discussion started: 21 October 2025

References

Adler, R. F., Huffman, G. J., Chang, A., Ferraro, R., Xie, P.-P., Janowiak, J., Rudolf, B., Schneider, U., Curtis, S., Bolvin, D., et al.: The version-2 global precipitation climatology project (GPCP) monthly precipitation analysis (1979–present), Journal of hydrometeorology, 4, 1147–1167, 2003.

Bretherton, C. S., Henn, B., Kwa, A., Brenowitz, N. D., Watt-Meyer, O., McGibbon, J., Perkins, W. A., Clark, S. K., and Harris, L.: Correcting coarse-grid weather and climate models by machine learning from global storm-resolving simulations, Earth and Space Science Open Archive, p. 39, https://doi.org/10.1002/essoar.10507879.1, 2021.

CESM2: Pre-Processing Reanalyses Data, Tech. Rep. last access: 25 May 2025, NSF National Center for Atmospheric Research, https://ncar.github.io/CAM/doc/build/html/users_guide/physics-modifications-via-the-namelist.html#nudging, 2025.

E3SM Project, U.S. Department of Energy: Energy Exascale Earth System Model v2.0, https://github.com/E3SM-Project/E3SM/releases/tag/v2.0.0, 2021.

Emanuel, K.: Tropical cyclone activity and global climate, Nature, 426, 644–648, https://doi.org/10.1038/nature02188, 2004.

Eyring, V., Bony, S., Meehl, G. A., Senior, C. A., Stevens, B., Stouffer, R. J., and Taylor, K. E.: Overview of the Coupled Model Intercomparison Project Phase 6 (CMIP6) experimental design and organization, Geoscientific Model Development, 9, 1937–1958, https://doi.org/10.5194/gmd-9-1937-2016, 2016.

Feng, L., Smith, S. J., Braun, C., Crippa, M., Gidden, M. J., Hoesly, R., Klimont, Z., van Marle, M., van den Berg, M., and van der Werf, G. R.: The generation of gridded emissions data for CMIP6, Geoscientific Model Development, 13, 461–482, https://doi.org/10.5194/gmd-13-461-2020, 2020.

Gates, W. L., Boyle, J. S., Covey, C., Dease, C. G., Doutriaux, C. M., Drach, R. S., Fiorino, M., Gleckler, P. J., Hnilo, J. J., Marlais, S. M., Phillips, T. J., Potter, G. L., Santer, B. D., Sperber, K. R., Taylor, K. E., and Williams, D. N.: An Overview of the Results of the Atmospheric Model Intercomparison Project (AMIP I), Bulletin of the American Meteorological Society, 80, 29–56, https://doi.org/10.1175/1520-0477(1999)080<0029:AOOTRO>2.0.CO;2, 1999.

Gettelman, A. and Morrison, H.: Advanced two-moment bulk microphysics for global models, Part I: Off-line tests and comparison with other schemes, Journal of Climate, 28, 1268–1287, https://doi.org/10.1175/JCLI-D-14-00102.1, 2015.

Golaz, J.-C., Larson, V., and Cotton, W.: A PDF-Based Model for Boundary Layer Clouds. Part I: Method and Model Description, Journal of the Atmospheric Sciences, 59, 3540–3551, https://doi.org/10.1175/1520-0469(2002)059<3540:APBMFB>2.0.CO;2, 2002.

Golaz, J.-C., Caldwell, P. M., Van Roekel, L. P., Petersen, M. R., Tang, Q., Wolfe, J. D., Abeshu, G., Anantharaj, V., Asay-Davis, X. S., Bader, D. C., Baldwin, S. A., Bisht, G., Bogenschutz, P. A., Branstetter, M., Brunke, M. A., Brus, S. R., Burrows, S. M., Cameron-Smith, P. J., Donahue, A. S., Deakin, M., Easter, R. C., Evans, K. J., Feng, Y., Flanner, M., Foucar, J. G., Fyke, J. G., Griffin, B. M., Hannay, C., Harrop, B. E., Hoffman, M. J., Hunke, E. C., Jacob, R. L., Jacobsen, D. W., Jeffery, N., Jones, P. W., Keen, N. D., Klein, S. A., Larson, V. E., Leung, L. R., Li, H.-Y., Lin, W., Lipscomb, W. H., Ma, P.-L., Mahajan, S., Maltrud, M. E., Mametjanov, A., McClean, J. L., McCoy, R. B., Neale, R. B., Price, S. F., Qian, Y., Rasch, P. J., Reeves Eyre, J. E. J., Riley, W. J., Ringler, T. D., Roberts, A. F., Roesler, E. L., Salinger, A. G., Shaheen, Z., Shi, X., Singh, B., Tang, J., Taylor, M. A., Thornton, P. E., Turner, A. K., Veneziani, M., Wan, H., Wang, H., Wang, S., Williams, D. N., Wolfram, P. J., Worley, P. H., Xie, S., Yang, Y., Yoon, J.-H., Zelinka, M. D., Zender, C. S., Zeng, X., Zhang, C., Zhang, K., Zhang, Y., Zheng, X., Zhou, T., and Zhu, Q.: The DOE E3SM Coupled Model Version 1: Overview and Evaluation at Standard Resolution, Journal of Advances in Modeling Earth Systems, 11, 2089–2129, https://doi.org/https://doi.org/10.1029/2018MS001603, 2019.

https://doi.org/10.5194/egusphere-2025-4277
Preprint. Discussion started: 21 October 2025

Golaz, J.-C., Van Roekel, L. P., Zheng, X., Roberts, A. F., Wolfe, J. D., Lin, W., Bradley, A. M., Tang, Q., Maltrud, M. E., Forsyth, R. M., Zhang, C., Zhou, T., Zhang, K., Zender, C. S., Wu, M., Wang, H., Turner, A. K., Singh, B., Richter, J. H., Qin, Y., Petersen, M. R., Mametjanov, A., Ma, P.-L., Larson, V. E., Krishna, J., Keen, N. D., Jeffery, N., Hunke, E. C., Hannah, W. M., Guba, O., Griffin, B. M., Feng, Y., Engwirda, D., Di Vittorio, A. V., Dang, C., Conlon, L. M., Chen, C.-C.-J., Brunke, M. A., Bisht, G., Benedict, J. J., Asay-Davis, X. S., Zhang, Y., Zhang, M., Zeng, X., Xie, S., Wolfram, P. J., Vo, T., Veneziani, M., Tesfa, T. K., Sreepathi, S., Salinger, A. G., Reeves Eyre, J. E. J., Prather, M. J., Mahajan, S., Li, Q., Jones, P. W., Jacob, R. L., Huebler, G. W., Huang, X., Hillman, B. R., Harrop, B. E., Foucar, J. G., Fang, Y., Comeau, D. S., Caldwell, P. M., Bartoletti, T., Balaguru, K., Taylor, M. A., McCoy, R. B., Leung, L. R., and Bader, D. C.: The DOE E3SM Model Version 2: Overview of the Physical Model and Initial Model Evaluation, Journal of Advances in Modeling Earth Systems, 14, e2022MS003 156, https://doi.org/https://doi.org/10.1029/2022MS003156, 2022.

Hannah, W. M., Bradley, A. M., Guba, O., Tang, Q., Golaz, J.-C., and Wolfe, J.: Separating Physics and Dynamics Grids for Improved Computational Efficiency in Spectral Element Earth System Models, Journal of Advances in Modeling Earth Systems, 13, e2020MS002 419, https://doi.org/https://doi.org/10.1029/2020MS002419, 2021.

Herrington, A. R., Lauritzen, P. H., Reed, K. A., Goldhaber, S., and Eaton, B. E.: Exploring a Lower-Resolution Physics Grid in CAM-SE-CSLAM, Journal of Advances in Modeling Earth Systems, 11, 1894–1916, https://doi.org/https://doi.org/10.1029/2019MS001684, 2019.

Hersbach, H., Bell, B., Berrisford, P., Biavati, G., Horányi, A., Muñoz Sabater, J., Nicolas, J., Peubey, C., Radu, R., Rozum, I., Schepers, D., Simmons, A., Soci, C., Dee, D., and Thépaut, J.-N.: ERA5 hourly data on pressure levels from 1979 to present, https://doi.org/10.24381/cds.bd0915c6, accessed on 27-JAN-2022, 2018a.

Hersbach, H., Bell, B., Berrisford, P., Biavati, G., Horányi, A., Muñoz Sabater, J., Nicolas, J., Peubey, C., Radu, R., Rozum, I., Schepers, D., Simmons, A., Soci, C., Dee, D., and Thépaut, J.-N.: ERA5 hourly data on single levels from 1940 to present, https://doi.org/10.24381/cds.adbb2d47, accessed on 27-JAN-2022, 2018b.

Hersbach, H., Bell, B., Berrisford, P., Hirahara, S., Horányi, A., Muñz Sabater, J., Nicolas, J., Peubey, C., Radu, R., Schepers, D., Simmons, A., Soci, C., Abdalla, S., Abellan, X., Balsamo, G., Bechtold, P., Biavati, G., Bidlot, J., Bonavita, M., De Chiara, G., Dahlgren, P., Dee, D., Diamantakis, M., Dragani, R., Flemming, J., Forbes, R., Fuentes, M., Geer, A., Haimberger, L., Healy, S., Hogan, R. J., Hólm, E., Janisková, M., Keeley, S., Laloyaux, P., Lopez, P., Lupu, C., Radnoti, G., de Rosnay, P., Rozum, I., Vamborg, F., Villaume, S., and Thépaut, J.-N.: The ERA5 global reanalysis, Quarterly Journal of the Royal Meteorological Society, 146, 1999–2049, https://doi.org/https://doi.org/10.1002/qj.3803, 2020.

Hoesly, R. M., Smith, S. J., Feng, L., Klimont, Z., Janssens-Maenhout, G., Pitkanen, T., Seibert, J. J., Vu, L., Andres, R. J., Bolt, R. M., Bond, T. C., Dawidowski, L., Kholod, N., Kurokawa, J.-I., Li, M., Liu, L., Lu, Z., Moura, M. C. P., O'Rourke, P. R., and Zhang, Q.: Historical (1750–2014) anthropogenic emissions of reactive gases and aerosols from the Community Emissions Data System (CEDS), Geoscientific Model Development, 11, 369–408, https://doi.org/10.5194/gmd-11-369-2018, 2018.

Huffman, G. J. and Bolvin, D. T.: TRMM and other data precipitation data set documentation, NASA Global Change Master Directory Doc., 44pp., NASA, Greenbelt, USA, ftp://precip.gsfc.nasa.gov/pub/trmmdocs/3B42_3B43_doc.pdf, 2015.

Iacono, M. J., Delamere, J. S., Mlawer, E. J., Shephard, M. W., Clough, S. A., and Collins, W. D.: Radiative forcing by long–lived greenhouse gases: Calculations with the AER radiative transfer models, Journal of Geophysical Research: Atmospheres, 113, D13 103, https://doi.org/10.1029/2008JD009944, 2008.

https://doi.org/10.5194/egusphere-2025-4277
Preprint. Discussion started: 21 October 2025

Jeuken, A. B. M., Siegmund, P. C., Heijboer, L. C., Feichter, J., and Bengtsson, L.: On the potential of assimilating meteorological analyses in a global climate model for the purpose of model validation, Journal of Geophysical Research: Atmospheres, 101, 16 939–16 950, https://doi.org/10.1029/96JD01218, 1996.

Kato, S., Rose, F. G., Rutan, D. A., Thorsen, T. J., Loeb, N. G., Doelling, D. R., Huang, X., Smith, W. L., Su, W., and Ham, S.-H.: Surface Irradiances of Edition 4.0 Clouds and the Earth's Radiant Energy System (CERES) Energy Balanced and Filled (EBAF) Data Product, Journal of Climate, 31, 4501 – 4527, https://doi.org/10.1175/JCLI-D-17-0523.1, 2018.

Knapp, K. R., Kruk, M. C., Levinson, D. H., Diamond, H. J., and Neumann, C. J.: The International Best Track Archive for Climate Stewardship (IBTrACS): Unifying Tropical Cyclone Data, Bulletin of the American Meteorological Society, 91, 363–376, https://doi.org/10.1175/2009BAMS2755.1, 2010.

Kooperman, G. J., Pritchard, M. S., Ghan, S. J., Wang, M., Somerville, R. C. J., and Russell, L. M.: Constraining the influence of natural variability to improve estimates of global aerosol indirect effects in a nudged version of the Community Atmosphere Model 5, Journal of Geophysical Research: Atmospheres, 117, D23 204, https://doi.org/10.1029/2012JD018588, 2012.

Larson, V. E., Golaz, J.-C., and Cotton, W. R.: A PDF-Based Model for Boundary Layer Clouds. Part I: Method and Model Description, Journal of the Atmospheric Sciences, 59, 3519–3539, https://doi.org/10.1175/1520-0469(2002)059<3519:SSAMVI>2.0.CO;2, 2002.

Lauritzen, P. H., Nair, R. D., Herrington, A. R., Callaghan, P., Goldhaber, S., Dennis, J. M., Bacmeister, J. T., Eaton, B. E., Zarzycki, C. M., Taylor, M. A., Ullrich, P. A., Dubos, T., Gettelman, A., Neale, R. B., Dobbins, B., Reed, K. A., Hannay, C., Medeiros, B., Benedict, J. J., and Tribbia, J. J.: NCAR Release of CAM-SE in CESM2.0: A Reformulation of the Spectral Element Dynamical Core in Dry-Mass Vertical Coordinates With Comprehensive Treatment of Condensates and Energy, Journal of Advances in Modeling Earth Systems, 10, 1537–1570, https://doi.org/https://doi.org/10.1029/2017MS001257, 2018.

Leung, L. R., Bader, D. C., Taylor, M. A., and McCoy, R. B.: An Introduction to the E3SM Special Collection: Goals, Science Drivers, Development, and Analysis, Journal of Advances in Modeling Earth Systems, 12, e2019MS001 821, https://doi.org/https://doi.org/10.1029/2019MS001821, 2020.

Lin, G., Wan, H., Zhang, K., Qian, Y., and Ghan, S. J.: Can nudging be used to quantify model sensitivities in precipitation and cloud forcing?, Journal of Advances in Modeling Earth Systems, 8, 1073–1091, https://doi.org/10.1002/2016MS000659, 2016.

Liu, X., Ma, P.-L., Wang, H., Tilmes, S., Singh, B., Easter, R. C., Ghan, S. J., and Rasch, P.: Description and evaluation of a new four–mode version of the Modal Aerosol Module (MAM4) within version 5.3 of the Community Atmosphere Model, Geoscientific Model Development, 9, 505–522, https://doi.org/doi.org/10.5194/gmd-9-505-2016, 2016.

Lo, J. C.-F., Yang, Z.-L., and Pielke Sr., R. A.: Assessment of three dynamical climate downscaling methods using the Weather Research and Forecasting (WRF) model, Journal of Geophysical Research: Atmospheres, 113, https://doi.org/https://doi.org/10.1029/2007JD009216, 2008.

Lohmann, U. and Hoose, C.: Sensitivity studies of different aerosol indirect effects in mixed-phase clouds, Atmospheric Chemistry and Physics, 9, 8917–8934, https://doi.org/10.5194/acp-9-8917-2009, 2009.

Ma, H.-Y., Chuang, C. C., Klein, S. A., Lo, M.-H., Zhang, Y., Xie, S., Zheng, X., Ma, P.-L., Zhang, Y., and Phillips, T. J.: An improved hindcast approach for evaluation and diagnosis of physical processes in global climate models, Journal of Advances in Modeling Earth Systems, 7, 1810–1827, https://doi.org/https://doi.org/10.1002/2015MS000490, 2015.

Mlawer, E. J., Taubman, S. J., Brown, P. D., Iacono, M. J., and Clough, S. A.: Radiative transfer for inhomogeneous atmospheres: RRTM, a validated correlated?k model for the longwave, Journal of Geophysical Research: Atmospheres, 102, 16,663–16,682, https://doi.org/10.1029/97JD00237, 1997.

https://doi.org/10.5194/egusphere-2025-4277
Preprint. Discussion started: 21 October 2025

Morrison, H. and Gettelman, A.: A New Two-Moment Bulk Stratiform Cloud Microphysics Scheme in the Community Atmosphere Model, Version 3 (CAM3). Part I: Description and Numerical Tests, Journal of Climate, 21, 3642–3659, https://doi.org/10.1175/2008JCLI2105.1, 2008.

NOAA GFDL: The GFDL Finite-Volume Cubed-Sphere Dynamical Core: Technical Description, Tech. rep., NOAA Geophysical Fluid Dynamics Laboratory, https://www.gfdl.noaa.gov/wp-content/uploads/2020/02/FV3-Technical-Description.pdf, 2020.

Oleson, K. W., Lawrence, M., Bonan, B., Drewniak, B. A., Huang, M., Koven, D., Levis, S., Li, F., Riley, J. P., Subin, M. C., Swenson, S. C., Thornton, E., Bozbiyik, A., Fisher, R. A., Heald, L., Kluzek, E., Lamarque, J., Lawrence, J., Leung, R., Lipscomb, W. H., Muszala, P., Ricciuto, M., Sacks, J., Sun, Y., Tang, J., and Yang, Z.: Technical description of version 4.5 of the Community Land Model (CLM), NCAR Technical Note NCAR/TN-503+STR, 420pp., NCAR, USA, https://doi.org/10.5065/D6RR1W7M, 2013.

Rasch, P. J., Xie, S., Ma, P.-L., Lin, W., Wang, H., Tang, Q., Burrows, S. M., Caldwell, P., Zhang, K., Easter, R. C., Cameron-Smith, P., Singh, B., Wan, H., Golaz, J.-C., Harrop, B. E., Roesler, E., Bacmeister, J., Larson, V. E., Evans, K. J., Qian, Y., Taylor, M., Leung, L. R., Zhang, Y., Brent, L., Branstetter, M., Hannay, C., Mahajan, S., Mametjanov, A., Neale, R., Richter, J. H., Yoon, J.-H., Zender, C. S., Bader, D., Flanner, M., Foucar, J. G., Jacob, R., Keen, N., Klein, S. A., Liu, X., Salinger, A., Shrivastava, M., and Yang, Y.: An Overview of the Atmospheric Component of the Energy Exascale Earth System Model, Journal of Advances in Modeling Earth Systems, 11, 2377–2411, https://doi.org/10.1029/2019MS001629, 2019.

Reynolds, R. W., Rayner, N. A., Smith, T. M., Stokes, D. C., and Wang, W.: An Improved In Situ and Satellite SST Analysis for Climate, Journal of Climate, 15, 1609–1625, https://doi.org/10.1175/1520-0442(2002)015<1609:AIISAS>2.0.CO;2, 2002.

Rutz, J. J., Shields, C. A., Lora, J. M., Payne, A. E., Guan, B., Ullrich, P., et al.: The Atmospheric River Tracking Method Intercomparison Project (ARTMIP): Quantifying Uncertainties in Atmospheric River Climatology, Journal of Geophysical Research: Atmospheres, 124, 13 777–13 802, https://doi.org/10.1029/2019JD030936, 2019.

Separovic, L., de Elía, R., and Laprise, R.: Impact of spectral nudging and domain size in studies of RCM response to parameter modification, Climate dynamics, 38, 1325–1343, https://doi.org/10.1007/s00382-011-1072-7, 2012.

Sun, J., Zhang, K., Wan, H., Ma, P.-L., Tang, Q., and Zhang, S.: Impact of Nudging Strategy on the Climate Representativeness and Hindcast Skill of Constrained EAMv1 Simulations, Journal of Advances in Modeling Earth Systems, 11, 3911–3933, https://doi.org/10.1029/2019MS001831, 2019.

Ullrich, P.: TempestExtremes v2.2.1, [Computer Software] https://github.com/ClimateGlobalChange/tempestextremes/releases/tag/v2.2.1, https://github.com/ClimateGlobalChange/tempestextremes/releases/tag/v2.2.1, 2022.

Ullrich, P. A., Zarzycki, C. M., McClenny, E. E., Pinheiro, M. C., Stansfield, A. M., and Reed, K. A.: TempestExtremes v2.1: a community framework for feature detection, tracking, and analysis in large datasets, Geoscientific Model Development, 14, 5023–5048, https://doi.org/10.5194/gmd-14-5023-2021, 2021.

Vincent, C. L. and Hahmann, A. N.: The Impact of Grid and Spectral Nudging on the Variance of the Near-Surface Wind Speed, Journal of Applied Meteorology and Climatology, 54, 1021 – 1038, https://doi.org/10.1175/JAMC-D-14-0047.1, 2015.

Wang, H., Easter, R. C., Zhang, R., Ma, P.-L., Singh, B., Zhang, K., Ganguly, D., Rasch, P. J., Burrows, S. M., Ghan, S. J., Lou, S., Qian, Y., Yang, Y., Feng, Y., Flanner, M., Leung, L. R., Liu, X., Shrivastava, M., Sun, J., Tang, Q., Xie, S., and Yoon, J.-H.: Aerosols in the E3SM Version 1: New Developments and Their Impacts on Radiative Forcing, Journal of Advances in Modeling Earth Systems, 12, e2019MS001 851, https://doi.org/https://doi.org/10.1029/2019MS001851, 2020.

https://doi.org/10.5194/egusphere-2025-4277
Preprint. Discussion started: 21 October 2025

Wang, Y., Liu, X., Hoose, C., and Wang, B.: Different contact angledistributions for heterogeneous ice nucleation in the CommunityAtmospheric Model version 5,, Atmospheric Chemistry and Physics, 14, 10 411–10 430, https://doi.org/doi.org/10.5194/acp-14-10411-2014, 2014.

Watt-Meyer, O., Bretherton, C. S., Gentine, P., Harris, L. M., and Toms, B. A.: Correcting Weather and Climate Models by Machine Learning Nudged Historical Simulations, Geophysical Research Letters, 48, e2021GL093 814, https://doi.org/10.1029/2021GL093814, 2021.

Wehrli, K., Guillod, B. P., Hauser, M., Leclair, M., and Seneviratne, S. I.: Assessing the Dynamic Versus Thermodynamic Origin of Climate Model Biases, Geophysical Research Letters, 45, 8471–8479, https://doi.org/https://doi.org/10.1029/2018GL079220, 2018.

Wehrli, K., Guillod, B. P., Hauser, M., Leclair, M., and Seneviratne, S.: Identifying Key Driving Processes of Major Recent Heat Waves, Journal of Geophysical Research: Atmospheres, 124, 11 746–11 765, https://doi.org/https://doi.org/10.1029/2019JD030635, 2019.

Wehrli, K., Luo, F., Hauser, M., Shiogama, H., Tokuda, D., Kim, H., Coumou, D., May, W., Le Sager, P., Selten, F., Martius, O., Vautard, R., and Seneviratne, S. I.: The ExtremeX global climate model experiment: investigating thermodynamic and dynamic processes contributing to weather and climate extremes, Earth System Dynamics, 13, 1167–1196, https://doi.org/10.5194/esd-13-1167-2022, 2022.

WMO: Global Guide to Tropical Cyclone Forecasting: Tropical Cyclone Operational Plan for the Western North Pacific and the South China Sea, https://community.wmo.int/en/activity-areas/tropical-cyclones, wMO-No. 1198, 2017.

Xie, S., Lin, W., Rasch, P. J., Ma, P.-L., Neale, R., Larson, V. E., Qian, Y., Bogenschutz, P. A., Caldwell, P., Cameron-Smith, P., Golaz, J.-C., Mahajan, S., Singh, B., Tang, Q., Wang, H., Yoon, J.-H., Zhang, K., and Zhang, Y.: Understanding Cloud and Convective Characteristics in Version 1 of the E3SM Atmosphere Model, Journal of Advances in Modeling Earth Systems, 10, 2618–2644, https://doi.org/https://doi.org/10.1029/2018MS001350, 2018.

Zhang, G. J. and McFarlane, N. A.: Sensitivity of climate simulations to the parameterization of cumulus convection in the Canadian Climate Centre general circulation model, Atmos. Ocean, 33, 407–446, https://doi.org/10.1080/07055900.1995.9649539, 1995.

Zhang, K., O'Donnell, D., Kazil, J., Stier, P., Kinne, S., Lohmann, U., Ferrachat, S., Croft, B., Quaas, J., Wan, H., Rast, S., and Feichter, J.: The global aerosol-climate model ECHAM-HAM, version 2: sensitivity to improvements in process representations, Atmospheric Chemistry and Physics, 12, 8911–8949, https://doi.org/10.5194/acp-12-8911-2012, 2012.

Zhang, K., Wan, H., Liu, X., Ghan, S. J., Kooperman, G. J., Ma, P.-L., Rasch, P. J., Neubauer, D., and Lohmann, U.: Technical Note: On the use of nudging for aerosol-climate model intercomparison studies, Atmospheric Chemistry and Physics, 14, 8631–8645, https://doi.org/10.5194/acp-14-8631-2014, 2014.

Zhang, S.: E3SM Model Code for Zhang et. al. (2025), https://doi.org/10.5281/zenodo.16815018, 2025a.

Zhang, S.: Analysis scripts and dataset for Zhang et. al. (2025), https://doi.org/10.5281/zenodo.17015705, 2025b.

Zhang, S., Zhang, K., Wan, H., and Sun, J.: Further improvement and evaluation of nudging in the E3SM Atmosphere Model version 1 (EAMv1): simulations of the mean climate, weather events, and anthropogenic aerosol effects, Geoscientific Model Development, 15, 6787–6816, https://doi.org/10.5194/gmd-15-6787-2022, 2022a.

Zhang, S., Zhang, K., Wan, H., and Sun, J.: Further improvement and evaluation of nudging in the E3SM Atmosphere Model version 1 (EAMv1): simulations of the mean climate, weather events, and anthropogenic aerosol effects, Geoscientific Model Development, 15, 6787–6816, https://doi.org/10.5194/gmd-15-6787-2022, 2022b.

Zhang, S., Harrop, B., Leung, L. R., Charalampopoulos, A.-T., Barthel Sorensen, B., Xu, W., and Sapsis, T.: A Machine Learning Bias Correction on Large-Scale Environment of High-Impact Weather Systems in E3SM Atmosphere Model, Journal of Advances in Modeling Earth Systems, 16, e2023MS004 138, https://doi.org/https://doi.org/10.1029/2023MS004138, 2024.